UNIVERSITY OF CALIFORNIA,
IRVINE

The effect of heat treatments on the microstructure and hardness of hot-work chromium tool steel manufactured by wire arc additive manufacturing

THESIS

submitted in partial satisfaction of the requirements
for the degree of

MASTER OF SCIENCE

in Materials Science and Engineering

by

Taiki Thomas Shirai

Thesis Committee:
Professor Diran Apelian, Chair
Professor Lorezno Valdevit
Professor Daniel R. Mumm

2022

TABLE OF CONTENTS

LIST OF FIGURES

LIST OF TABLES

ACKNOWLEDGEMENTS

Firstly, I would like to express the deepest appreciation to my committee chair, Professor Diran Apelian for providing me with this opportunity and for guiding me through this thesis research. Not only has Diran taught me more about metallurgy, but also how to be a better presenter and how to be a better human being. I am forever grateful to Diran for teaching me these skills.

I would also like to thank my committee members, Professor Lorenzo Valdevit and Professor Daniel Mumm for their input whether it be in group meetings or in the classroom I have learned much on how to better present my research.

In addition, I would like to express my gratitude to Dr. Carl Söderhjelm for guiding me on this thesis research and writing process. Carl's questions have reshaped my decision-making process as a researcher. As an engineer and as a researcher I feel I have grown immensely under Carl's mentorship, and I am grateful for the opportunity to work with someone like him.

I would also like to express my gratitude to Gerald Anzalone from Michigan Technological University for printing the samples used in this thesis research, and Patricia Miller from Uddeholm for her advice on characterization for this research. I learned much about welding and ferrous metallurgy from them two.

I would also like to express my gratitude to the members of Diran's group with whom I have had the opportunity to work with over the past year. Shri, Calvin, Dr. Benjamin Macdonald, Sam, Raquel, Brandon, Sakshi, Mahsa, Ryan, and Cheolmin you all have had an impact on this thesis research either directly or indirectly, and for that I say thank you! I hope we cross paths again in the future whether in the workplace or in a casual setting.

Lastly, I want to thank my parents, friends, and former colleagues for their constant support this past year. I would not be here without everyone's support.

ABSTRACT OF THE THESIS

The effect of heat treatments on the microstructure and hardness of hot-work chromium tool steels manufactured by wire arc additive manufacturing

by

Taiki Thomas Shirai

Master of Science in Materials Science and Engineering

University of California, Irvine, 2022

Professor Diran Apelian, Chair

High pressure die casting remains a fast, cost-effective technique for manufacturing complex automotive parts. The harsh working conditions that the molds endure make them susceptible to corrosion and thermal fatigue. The metals utilized in molds are often expensive and difficult to machine, necessitating proper maintenance to extend their lifespans. Straight cooling channels in molds have been effective in extending the lifespans of these molds by managing the temperature of vulnerable spots. However, straight channels are ineffective when cooling complex geometries. In recent years, additive manufacturing (AM) has been deemed a promising solution due to its ability to create near net shape parts with complex internal geometries. Leveraging this ability, complex cooling channels can be created that conform to the geometry of the mold. Research has been done on the additive manufacturing of a popular mold material, H13 tool steel, using laser powder bed fusion. Unfortunately, the resulting parts have issues with cracks and delamination from the substrate plate.

An emerging AM technique known as wire arc additive manufacturing (WAAM) has demonstrated its ability to print H13 tool steel without cracks. Although successful, no work has been done on heat treating these as-built structures to achieve the desired microstructure needed

for use in high pressure die casting applications. In addition, most of the research has been done solely on H13. In this study, H13 tool steel and two other hot-work chromium tool steels were manufactured with WAAM and subjected to a conventional heat treatment consisting of: annealing, austenitizing, and tempering. Due to the high hardness of the as-built condition, samples were also taken directly through a tempering cycle after printing to determine the viability of reducing the post processing time by more than 30 hours. The microstructures after each heat treatment condition were analyzed and hardness tested. Despite their microstructural differences when compared to the wrought state, the tool steels studied were able to be heat treated conventionally and directly from the as-built condition to a desired range of 44 to 48. The size of the alloy carbides strongly influenced the hardness of each tool steel after each heat treatment.

Chapter 1: Introduction

1.1 Additive Manufacturing

Additive manufacturing (AM) is a process in which a three-dimensional object is built layer by layer. Three-dimensional objects are designed with computer aided design (CAD) and processed where the design is broken down a file layer-by-layer. A machine reads the layer-by-layer file to manufacture the object. AM has several advantages. Since AM is based on CAD files, anything that can be designed in CAD can be manufactured. Complex shapes with intricate geometries that are impossible to attain with conventional manufacturing processes can be easily created using AM. With this, multiple parts can be re-designed as one to reduce the overall number of parts required for the assembly of a larger component [1]. For example using AM, General Electric was able to reduce the part count on their fuel nozzle from 20 parts to a single part as seen in Figure 1 [2]. This resulted in cost savings and eliminated the assembly of this fuel nozzle, thus reducing manufacturing and lead times. Objects manufactured by AM are near net shape, eliminating the need for extensive post process machining. Expensive, difficult to machine materials such as titanium and hardened steels are of interest to save on machining time and expensive equipment. While post-processing is still required for parts manufactured by AM due to its step-wise surface finish, the scrap is significantly reduced. Parts manufactured conventionally can yield scrap ratios up to 90% while parts manufactured by additive technologies can yield scrap ratios up to 10% [3]. Parts can be produced on demand by AM so long as feedstock materials are available. This advantage was highlighted when the world's supply chain fell apart during the COVID-19 pandemic, as businesses struggled to acquire the necessary parts needed to continue their production. Businesses shifted their attention to AM as a

remedy to their supply chain issues. This shift has industry and researchers heavily invested in AM to hasten its maturation as a viable production process.

Figure 1: GE fuel nozzle [2].

With the growing interest in additive manufacturing numerous techniques have been developed over the past decade. The joint classification by the International Standards Organization and the American Society of Testing and Materials (ISO/ASTM 52900:2015) classifies these techniques into seven broad categories: binder jetting, directed energy deposition, material extrusion, material jetting, powder bed fusion, sheet lamination, and vat photopolymerization [4]. These categories can be further classified by their feedstock material or their energy source. Several of these techniques can process materials such as ceramics, polymers, and metals. A significant area of interest by universities and industry has been in the processing of metals with AM. The techniques utilized in metal AM are binder jetting, directed energy deposition, powder bed fusion, and a technique not captured by the ASTM classification known as cold spray, a solid-state deposition process which relies on metallurgical bonding and mechanical interlocking caused by the plastic deformation of powders upon impact [5]. A bulk of research in metal AM has focused on powder bed fusion. However, due to its restrictions on

build volume and low deposition rate its applications are limited. While there have been many efforts to increase the deposition rate of powder bed fusion, directed energy deposition (DED) overcomes these limitations. DED is a process in which a focused heat source melts feedstock material as it is deposited [6]. DED can be further subdivided based on its type of feedstock material and heat source.

1.2 Wire Arc Additive Manufacturing

A technique similar in concept to DED that has gained recent attention is wire arc additive manufacturing (WAAM). WAAM draws technology from traditional arc welding processes such as gas metal arc welding (GMAW), gas tungsten arc welding (GTAW), and plasma arc welding (PAW). Instead of joining pieces, the electric arc is used to melt wire feedstock on to a substrate and previously deposited layers to form a three-dimensional object. Figure 2 displays a simple schematic of the WAAM process.

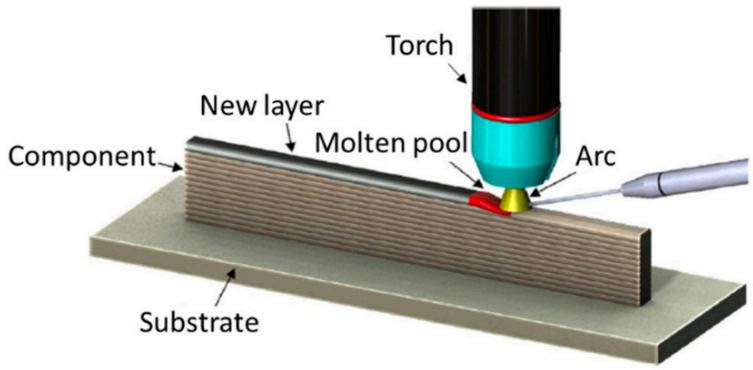

Figure 2: Schematic of wire arc additive manufacturing process [7].

WAAM has been utilized as an AM process since the 1990's and systems used standard off the shelf welding equipment: welding power source, welding torch, and wire feeding systems [8]. A robotic system moves the torch and wire feeding system, allowing for the deposition of the melted material. In comparison to other metal AM processes, WAAM excels in deposition rate as shown in Figure 3. WAAM owes its high deposition rate to its ability to print at the largest

layer thicknesses of all the metal AM process as seen in Table 1. Its deposition rate falls in comparison to cold spray, but possesses better featural resolution. While cold spray possesses the highest deposition rate it is also limited to processing only ductile metals since it relies on the plasticity of the feedstock material. WAAM has the ability to handle any type of feedstock, even brittle metals. In addition, WAAM does not require a protective enclosure to operate, thus eliminating the restrictions on build volume.

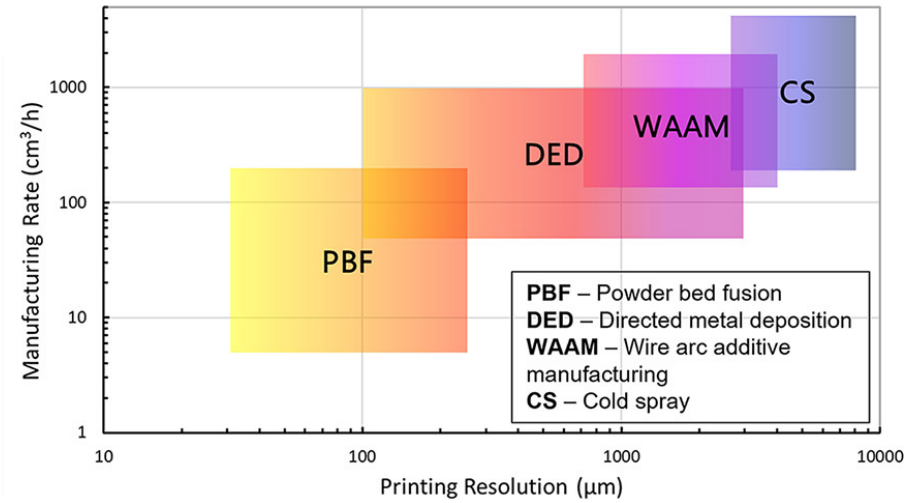

Figure 3: Comparison of deposition rates and resolution between metal AM techniques [9].

Table 1: Comparison of commonly studied metal AM techniques.

	DED	*LPBF*	*WAAM*	*Cold Spray*
Max layer thickness (µm)	500	100	2000	1000
Maximum Build volume (mm x mm x mm)	2000 x 1500 x 750	500 x 280 x 320	Theoretically Limitless	1000 x 1000 x 700
Surface Roughness (µm)	25	20	500	40
References	[6]	[10], [11]	[11]	[12]–[14]

With a high deposition rate and a theoretically limitless build volume, WAAM is extremely attractive for the production of large structures. An example of this can be seen in Figure 4 where MX3D constructed a 12-meter-long stainless-steel bridge in Amsterdam using WAAM [15].

Figure 4: MX3D Bridge in Amsterdam [15].

Despite its advantages, the electric arc used in WAAM produces an extensive amount of heat that cause previously deposited layers to reheat and form thermal stresses. In some cases, these stresses can exceed the yield stress of the material causing the part to delaminate and fail. Furthermore, due to the large layer thicknesses structures manufactured by WAAM, parts are often met with poor surface roughness. Ultimately, this necessitates post-machining and stress relief cycles on all WAAM parts to achieve quality parts. Expensive, difficult to machine materials such as titanium and hardened steels have been the focus of much research on WAAM due to its potential for cost and material savings. The research done in this work will focus on using WAAM to process one of these materials: tool steels.

1.3 Tool Steels

A tool steel is defined as any steel used to make cutting, forming, or shaping tools [16]. The major alloying elements in tool steels are tungsten, chromium, molybdenum, and vanadium. These elements react with carbon to form high temperature carbides that increase the hardness of the steels [16]. This is necessary since tool steels are subjected to extremely rapid, high loads and high temperatures. Tool steels that are involved with forming metals at high temperatures are known as hot work tool steels [17]. Hot work tool steels are heavily used in high pressure die

casting, where a piston transports molten metal at a high velocity into a steel die [18]. Due to the high temperature, high forces acting on the material there is a persistent desire to control the thermal conditions in order to decrease cycle time and extend the life of molds [19]. Decreasing cycle times and extending the lifetime of molds results in major cost savings. Straight line cooling channels have conventionally been introduced into molds through drilling [20]. However, these are ineffective especially on curved cavities since the distance between the cavity and the cooling line varies along its length as seen in Figure 5a, causing non-uniform cooling rates. Non-uniform cooling rates can cause some areas to accumulate heat and be vulnerable to thermal fatigue.

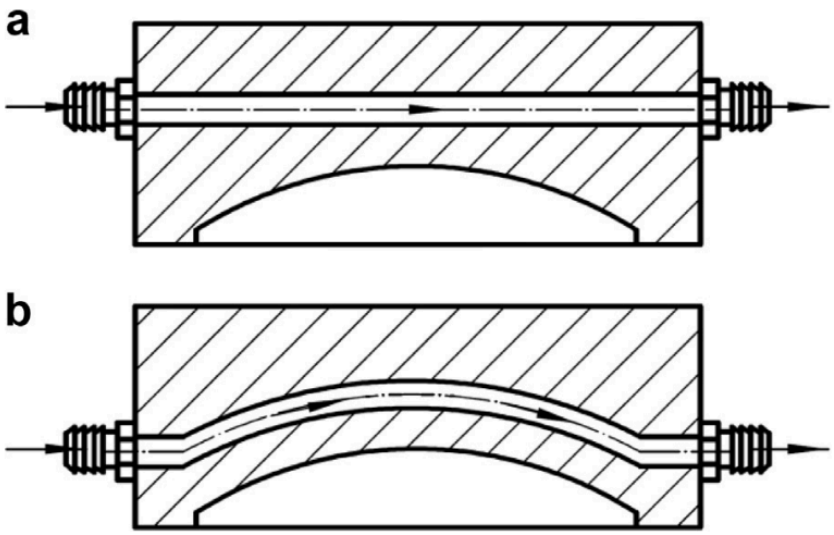

Figure 5: Schematic of (a) straight drilled cooling channel, (b) conformal cooling channel [21].

With the ability to create complex internal geometries, industry has looked to additive manufacturing to produce molds and dies with integrated cooling channels that conform to the mold geometry, known as conformal cooling channels. These channels would be designed to be equidistant with the features of the mold to provide uniform cooling rates across the cooling line as seen in Figure 5b. While much literature has printed hot work tool steels with laser powder bed fusion, a common issue is the formation of cracks in the printed microstructure [22].

In the limited literature on tool steels processed by WAAM cracking does not arise, making WAAM attractive for conformal cooling applications. Most of the literature focuses on H13. H13 has high hardness, toughness, and excellent thermal shock and fatigue resistance making it an ideal material for molds and dies for casting applications [23]. All of the work done with H13 report different microstructures. Wang et al. printed a thin wall of H13 tool steel and found an mixed microstructure of martensite and bainite [24]. The authors concluded this microstructure was caused by variations in local thermal history with no further elaboration. It is unclear from the manuscript what these local thermal histories are and how they influenced the formation of bainite and martensite in separate regions. The microstructures observed in H13 were further investigated by Ali et al. In their thin wall sample, the authors found a combination of martensite, retained austenite, and tempered martensite in the bulk of the sample, while the top was composed of martensite, carbides, and retained austenite [25]. They concluded this was due to the distribution of heat during remelting. Remelting occurs in AM since the heat produced by the heat source not only transfers to the feedstock material, but also to the substrate and previously deposited layers through conduction. Remelting increases the temperature of the lower layers to values above the martensite start temperature, initiating the transformation of retained austenite to martensite while also tempering the previously formed martensite, thus softening the layers [25]. Remelting also occurs in the overlap region between two depositions. Ge et al. studied the effect of remelting in the overlap region by printing a block specimen. In the overlap region the authors found ferrite and martensite, which contributed to fairly ductile tensile behavior [26]. This contrasted the research done by Hackenhaar et al. who evaluated the effect of three different deposition modes on the properties of H13. Hackenhaar et al. observed the same tensile behavior for the modes evaluated: brittle tensile behavior [27]. While much preliminary

work focused on room temperature mechanical properties, Tanvir et al. studied the performance of WAAM produced H13 at elevated temperatures. They discovered that these phases remain at 600 °C, but observed tensile properties below that of wrought values [28]. This is interesting since the authors are comparing as-built properties with wrought material that has undergone post processing heat treatment to attain a certain phase distribution. The as-built microstructures are expected to differ from wrought microstructures, so a difference in mechanical properties is expected. In order to truly compare wrought and WAAM processed tool steel the as-built samples should undergo a heat treatment to achieve the desired microstructure for use in high pressure die casting applications.

The conventional heat treatment process for tool steels is a multi-step process. First, parts are taken through an annealing step to promote the growth of softer phases: ferrite and cementite. This softens the parts for rough machining or cold working. After rough machining, parts are taken to above the austenite formation temperature (A_3) into the austenitizing region as seen in the iron carbon phase diagram in Figure 6 to transform the body-centered cubic to a fully face-centered cubic austenitic microstructure [29]. While at this high temperature the carbides begin to dissolve and carbon atoms diffuse into the iron matrix [30]. The parts are then quenched rapidly to initiate the martensite transformation for strengthening. During rapid quenching, carbon does have enough time to escape the interstitial sites in iron and subsequently remain in the lattice, causing the lattice to distort resulting in a change of crystal structure from a face-centered cubic to a body-centered tetragonal [30]. This transformation strains the crystal lattice. Since the martensite finish temperature is below room temperature, not all of the austenite is transformed to martensite. The remaining austenite after quenching is called retained austenite.

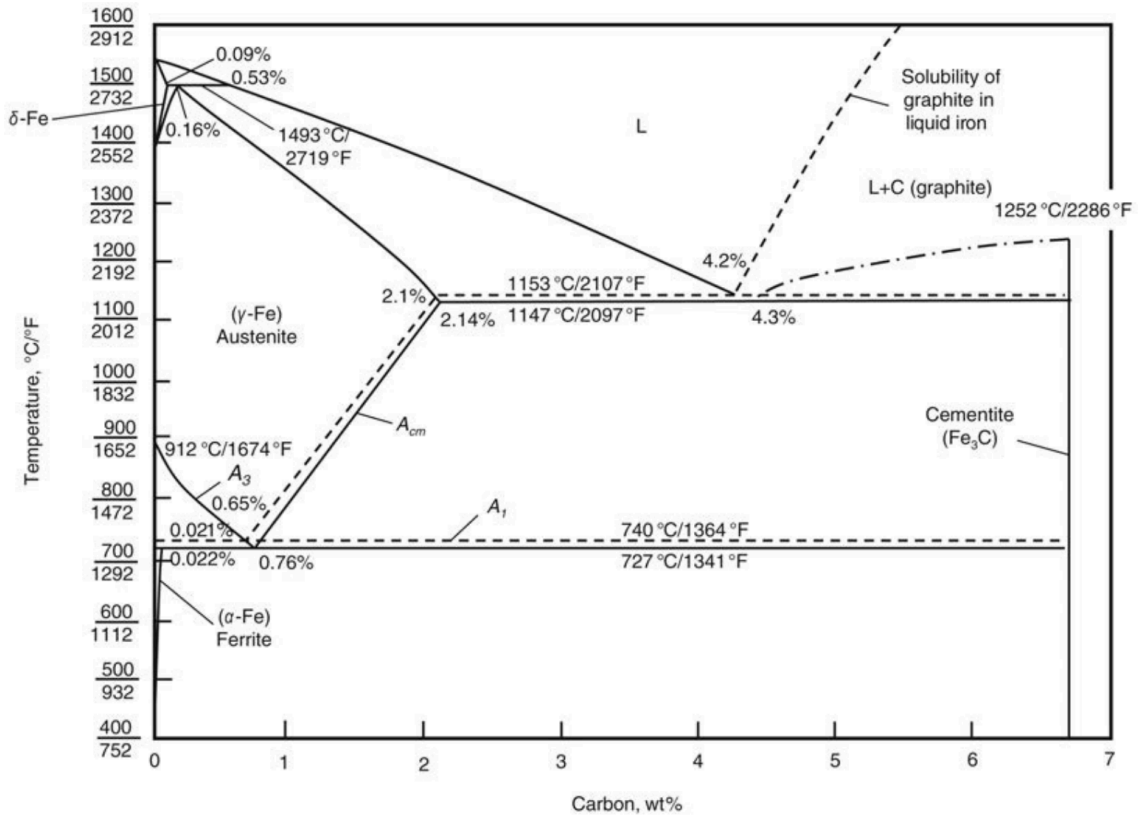

Figure 6: Iron-Carbon binary phase diagram [29].

After the part has cooled from austenitizing it is taken to a temperature below the critical temperature austenite formation temperature (A_1). This is known as a tempering cycle. Here interstitial carbon is allowed to diffuse out from the martensite to form alloy carbides or cementite; alleviating the strain on the lattice while improving the toughness of the material [31]. Upon quenching, retained austenite goes through martensitic transformation. A secondary temper is often used for applications where extremely low retained austenite content is required. Figure 7 displays the conventional heat treatment from start to finish.

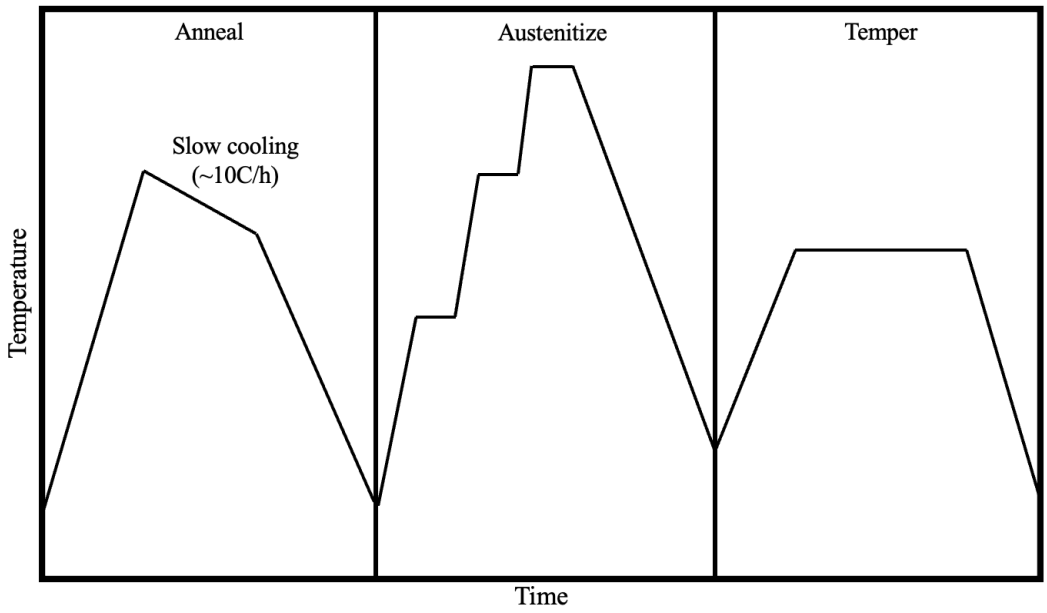

Figure 7: Conventional heat treatment process for tool steels.

This problem with the conventional heat treatment is its long duration. AM already suffers from slow manufacturing speeds so a long post-processing heat treatment cycle makes AM a less economically attractive manufacturing process [32]. Since AM produces structures at hardness values similar to what is observed after austenitizing, there is interest in understanding the feasibility of bypassing the annealing and austenitizing cycles and taking the as-built structure directly to tempering. Eliminating the annealing and austenitizing step would cut the post heat treatment time down by at least 30 hours or even more depending on the part geometry. Since tempering alleviates lattice stresses, directly tempering would aid in stress relieving parts manufactured by WAAM.

Therefore, the goal of this work is to understand the feasibility of taking tool steel parts manufactured by WAAM through both a conventional heat treatment like a wrought material, and a direct temper. The microstructure at each heat treatment step will be evaluated to understand how the as-built microstructure responds to each heat treatment. The final microstructures after a conventional heat treatment and a direct temper will be compared.

Wrought H13 will undergo the same heat treatments to compare and contrast with the tool steels manufactured by WAAM. This study will also aim to demonstrate the ability to print hot-work chromium tool steel other than H13.

Chapter 2: Materials and Experimental Methods

2.1 Materials

The H13 wire feedstock used in these experiments was provided by Eureka Welding Alloys. Eureka Welding Alloys names their H13 wires, Eureka 31. Two types of H13 wire feedstock were evaluated: cored and solid. The H13 cored wire is composed of a mild steel sheath and core filled with deoxidizers, arc stabilizers, and elemental powder that make up the H13 composition. Because of this, the price of the H13 cored wire from Eureka Welding Alloys is one-third the price of the H13 solid wire. Figure 8 displays cross sections of cored and solid wires for comparison. For comparison, wrought H13 was purchased from Tool Steel Service, Inc. The supplied wrought H13 was delivered in its annealed state so there will be no microstructural comparisons between the as-built condition and the wrought material.

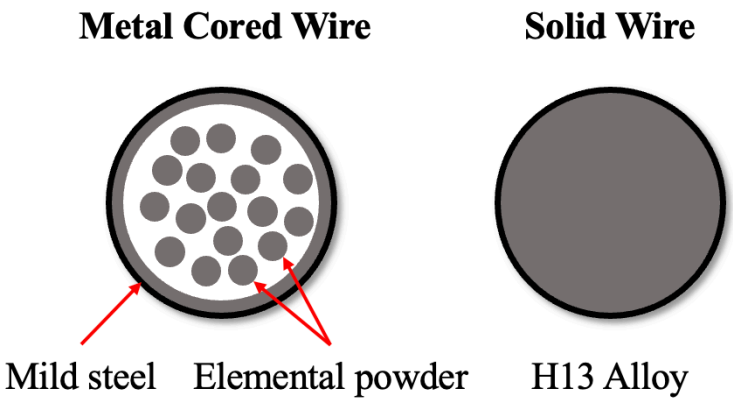

Figure 8: Cross sections of metal H13 cored wire and solid H13 wire.

Two additional hot work chromium tool steels were evaluated for their excellent properties in high pressure die casting systems: Dievar and QRO 90. These two feedstocks were provided by Uddeholm. Dievar is a premium hot work tool steel developed by Uddeholm that boasts excellent resistance to heat checking due to its superior ductility [33]. Heat checking is surface cracking that occurs from repeated thermal fluctuations that commonly occur during high pressure die casting [34]. QRO 90 is another premium hot work tool steel developed by

Uddeholm that boasts improved resistance to heat checking due to its excellent high temperature strength [35]. QRO 90 also possesses a higher thermal conductivity than other hot work tool steels, allowing for the possibility of reducing cycle times and increasing productivity [35]. Wrought forms of these Uddeholm materials were not able to be purchased in time to conduct a comparison, but is the subject of future work. A comparison of the chemical compositions is listed in Table 2 below. For consistency all wire feedstocks had a diameter of 1.2 mm.

Table 2: Chemical compositions of the hot work tool steels studied in this work.

	C	*Si*	*Mn*	*Cr*	*Mo*	*V*	*Fe*
H13 Cored [36]	0.35	0.80	0.80	5.00	1.50	1.00	Bal
H13 Solid [37]	0.35	0.80	0.80	5.00	1.50	1.00	Bal
Dievar [33]	0.35	0.20	0.50	5.00	2.30	0.60	Bal
QRO 90 [35]	0.38	0.30	0.75	2.60	2.25	0.90	Bal

2.2 Experimental Methods

Samples of each material were manufactured using a custom WAAM system developed by Michigan Technological University. The system consists of a S350 Advanced Process Welder power source from Lincoln Electric, Power Feed 25M Semi-Automatic Wire Feeder wire feeder from Lincoln Electric, that are attached to a 3-axis CNC machine as shown in Figure 9. A part of their custom WAAM system is a unique proprietary substrate plate. This along with a custom print head are blocked out and will not be further discussed.

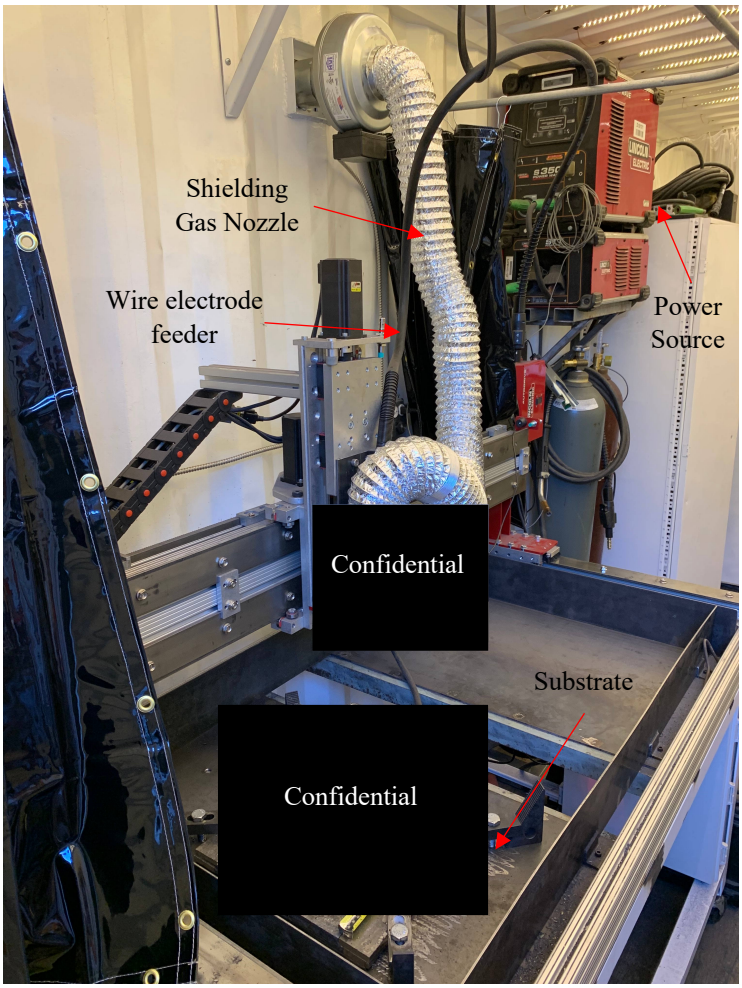

Figure 9: WAAM system setup at Michigan Technological University.

Lincoln Electric's Surface Tension Transfer® (STT) process was utilized. STT welding is a Lincoln Electric developed short circuit transfer version of the GMAW process. In STT, only current is adjusted to control the heat input. An initial background current is established to heat the base metal and establish the arc. After the electrode contacts with the molten pool, the current is reduced to ensure short circuiting. The current is then steadily ramped, this is known as a pinch current, to initiate the separation between the metal droplet and the electrode. Right before separation the current is reduced to induce droplet transfer to the substrate. Once the arc is re-established, a high peak current is applied to push down the weld pool to prevent shorting and to heat the deposition. The current exponentially decreases or tails out to the background current to

regulate thermal input [38]. Figure 10 graphically displays the changes in current during STT. By reducing the current at different times during the deposition process, the overall heat input of the process is reduced. A lower heat input can reduce residual stresses, spatter, and solidification defects.

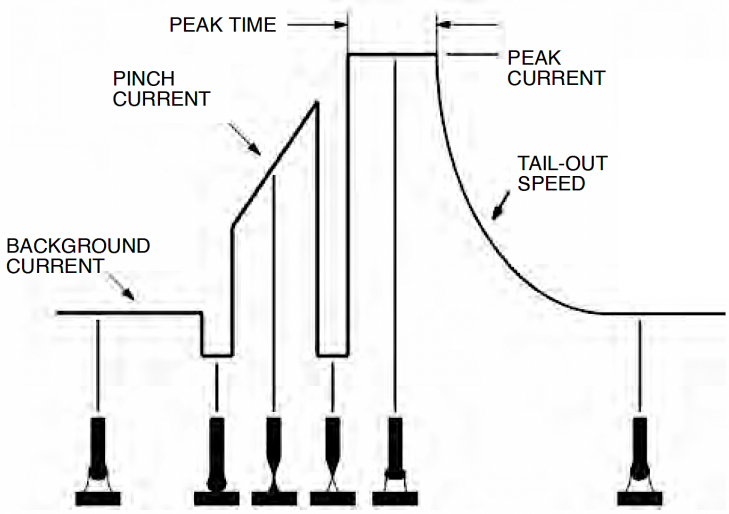

Figure 10: Graphical depiction of current values during the STT process [38].

Due to the vast changes in current, it was not recorded. The collaborators also wished to keep the welding parameters confidential. The unique mild steel substrate was not preheated and 100% industrial grade argon was used as a shielding gas. To create an 85 mm × 15 mm × 110 mm sample, the deposition of each layer started at (0, 0, z) on to the proprietary mild steel substrate. A single continuous bead that traced the perimeter of sample was deposited followed by a straight, continuous bead to fill in the inside. Figure 11 displays the deposition path. Prior to the deposition of the next layer, the electrode moves back to the origin and raises a specified z height. There was no dwell time between layers. The printed samples of H13 Cored, H13 Solid, Dievar, and QRO 90 are displayed in Figure 12(a), (b), (c), and (d) respectively.

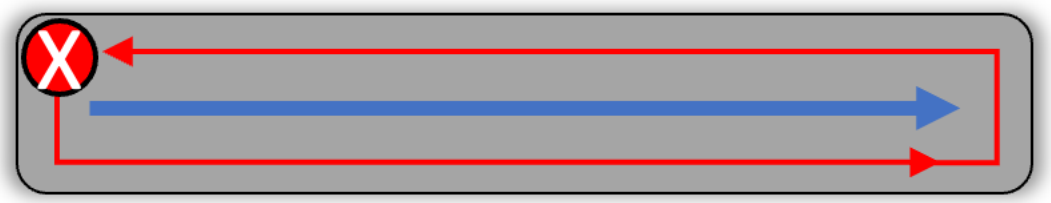

Figure 11: Deposition path used to print the as-built samples. The X denotes the starting point for each layer. The red arrow represents the initial straight bead and the blue arrows represent the subsequent deposition along the perimeter of the first deposition.

Figure 12: Images of the as-deposited samples for (a) H13 Cored, (b) H13 Solid, (c) Dievar, and (d) QRO 90 produced by Michigan Technological University.

Samples were sectioned using the Buehler AbrasiveMet M for use in microstructure and mechanical property evaluation. Sections of the as-built walls were chemically analyzed using the SPECTROLAB S arc spark optical emission spectrometry (OES) to observe any changes in composition that may occur during the printing process. Three hardness measurements using the Rockwell C scale were taken along the height of the build with the Wilson Rockwell 574 machine to observe any variations. Prior to all heat treatments, samples were protected in stainless steel tool wrap with paper to mitigate decarburization. After quenching, all samples were lightly ground to remove any possible decarburization layer. H13 samples were annealed at 850 °C for 30 minutes and slow cooled at a rate of 30 °C/hour until a temperature of 432 °C, then quenched in still air. Dievar samples were annealed at 850 °C, slow cooled at a rate of 10 °C/hour until a temperature of 600 °C, and then quenched in still air. QRO 90 samples were annealed at 820 °C, slow cooled at a rate of 10 °C/hour until a temperature of 650 °C, and then quenched in still air. All annealing treatments took place in a Nabertherm convection furnace. After annealing, samples were austenitized at various temperatures between 1000 °C and 1050 °C with a Thermolyne 30400 muffle furnace. The temperatures trialed for each material is listed in Table 3 below. All of the annealed samples were preheated to 600 °C, 850 °C, then to the desired temperature to prevent thermal shock that may occur due to the change in volume when ferrite transforms to austenite [34]. Samples were soaked at temperature for 30 minutes and then quenched in still air. Austenitizing temperatures that would provide the as-built hardness were chosen based on curves from technical data sheets from an H13 database and Uddeholm. These curves are shown in Appendix A. Temperatures were varied to in case the different starting microstructure affected the response to austenitizing. After quenching, hardness was measured to identify which temperatures reached the as-built hardness.

Table 3: Temperatures used for the austenitizing trials (AT).

	AT1	*AT2*	*AT3*
H13 Cored	1010 °C	1030 °C	1050 °C
H13 Solid	1010 °C	1020 °C	1030 °C
Dievar	1000 °C	1010 °C	1020 °C
QRO 90	1010 °C	1020 °C	1030 °C

New sections were annealed, austenitized, for the tempering trials. Tempering temperatures that were expected to reach a hardness value within the range of 44 to 48 Rockwell C were chosen based on curves from technical data sheets from Eureka Welding Alloys and Uddeholm. These curves are shown in Appendix B. As-built samples were subjected to the same tempering temperatures as in Table 4. After tempering, all samples underwent hardness testing.

Table 4: Temperatures used for the tempering trials (T).

	T1	*T2*	*T3*
H13 Cored	615 °C	625 °C	635 °C
H13 Solid	615 °C	625 °C	635 °C
Dievar	580 °C	600 °C	620 °C
QRO90	610 °C	630 °C	650 °C

All of the samples from each heat treatment step were mounted in phenolic mounting powder by the Buehler Simplimet 4000 hot mounting system. Samples were ground, then polished to mirror like finishes using the Buehler AutoMet 250. Samples were etched using a solution of 2% Nital reagent, rinsed in deionized water, and then in 4% Picral reagent to evaluate the phases produced from each heat treatment step. Etching times varied between samples and was done until the microstructure was observed. Images were taken at 2000X using the Evident Scientific digital microscope to view microstructural features.

Chapter 3: Results and Discussion

3.1 Evaluation of the as-built condition

Table 5 displays the expected and measured chemical composition of each tool steel in the as-built condition. The expected chemical compositions were taken from technical data sheets provided by Eureka Welding Alloys and Uddeholm. The as-built H13 cored sample showed no major differences in chemical composition from its expected values. The silicon content is slightly higher than the expected value but is still within the acceptable range set by ASTM A681-08 [39]. The silicon content for H13 can be as high as 1.25 wt%. The as-built H13 solid sample showed some significant differences. The measured manganese content is lower than expected. Manganese losses have been observed in welding of steels since its vapor pressure is much higher than that of iron so it has a greater tendency to evaporate [40]. The power inputted into the deposition of the H13 solid sample may be too high and cause evaporation of the manganese. Since there was no dwell time, manganese evaporation could happen. The major alloying elements in the as-built Dievar did not vary significantly from its expected chemical composition. The as-built QRO 90 sample deviated greatly from its expected chemical composition. Silicon, manganese, and molybdenum were measured higher than expected. A conversation with Uddeholm revealed that these elements are intentionally raised in their QRO 90 wires so that the tempering curve of base material and wire match when the weld rod is welded to QRO90. The measured values for those elements in QRO 90 were expected.

Table 5: Comparison between the expected chemical compositions from technical data sheets and chemical compositions measured via OES for H13 Cored, H13 Solid, Dievar, and QRO 90. The measured values in green are within the specification while the values in red are outside the specification.

		C	*Si*	*Mn*	*Cr*	*Mo*	*V*	*Cu*	*Fe*
H13 Cored	Expected [36]	0.35	0.80	0.80	5.00	1.50	1.00	<0.10	Bal
	Measured	0.35	1.02	0.76	5.00	1.43	1.04	0.04	Bal
H13 Solid	Expected [37]	0.35	0.80	0.80	5.00	1.50	1.00	<0.10	Bal
	Measured	0.36	0.87	0.30	5.26	1.23	0.89	0.43	Bal
Dievar	Expected [33]	0.35	0.20	0.50	5.00	2.30	0.60	0.04	Bal
	Measured	0.30	0.18	0.41	5.12	2.38	0.51	0.85	Bal
QRO 90	Expected [35]	0.38	0.30	0.75	2.60	2.25	0.90	0.04	Bal
	Measured	0.30	0.85	1.30	2.85	2.89	0.87	0.34	Bal

While the major alloying elements were relatively within expectations, samples built from H13 solid, Dievar, and QRO 90 reported unexpected amounts of copper. The sample made of H13 cored wire feedstock showed minimal presence of copper. In order to understand if the presence of copper in these samples was a result of equipment error, wrought H13 was analyzed using ark spark OES. Table 6 compares the expected and measured chemical compositions of wrought H13. The measured chemical compositions of wrought H13 agree well with the expected composition.

Table 6: Comparison between expected chemical compositions from technical data sheets and chemical compositions measured via OES for wrought H13.

		C	*Si*	*Mn*	*Cr*	*Mo*	*V*	*Cu*	*Fe*
Wrought H13	Expected	0.40	1.05	0.42	5.20	1.28	0.95	<0.10	Bal
	Measured	0.38	0.98	0.39	5.01	1.29	0.91	0.06	Bal

A discussion with the collaborators at Michigan Technological University revealed that a copper coating was added to the H13 solid, Dievar, and QRO 90 wire feedstocks. Coating wires with copper is a common practice in traditional welding to improve the conductivity of the wire. The H13 cored wire feedstock was coated with graphite to improve its conductivity. Improved

conductivity allows for a more stable; a consistent arc reduces the formation of imperfections in the deposition [40]. As a result, the presence of copper in those three feedstocks are expected.

Literature suggests that copper content affects the microstructure of tool steels. In cold work tool steels, Kang et al. observed that the microstructure after austenitizing had an increased fraction of retained austenite resulting in a decreased hardness value. The authors theorized this was because copper stabilizes austenite so during quenching more austenite will be retained [41]. More retained austenite in the quenched condition means that during tempering the steel might experience hardening as more martensitic transformation occurs. A secondary temper becomes necessary to soften the newly formed martensite. The authors also observed that copper suppressed the formation of $M_{23}C_6$ carbide, affecting the strengthening this precipitates provides [41]. Unfortunately, no mechanical testing was done to understand the influence of these precipitates on the mechanical properties. From literature, it can be inferred that the microstructures of the wire feedstocks with copper will have contain more retained austenite.

After chemical analysis, hardness measurements were taken on the as-built condition along the height of the sample. In Figure 13, hardness measurements slightly increase along the build height for all four tool steels. This softening of lower layers is a result of reheating. During the deposition of a new layer, heat generated by the arc is applied to the feedstock. This heat also reheats previously deposited layers. The solidified layers reach a range of temperatures often depending on the distance from the new layer. Locations further away from the latest deposition may reach temperatures that cause grain and precipitate growth while locations closer to the latest deposition can experience temperatures above melting and re-solidify with the latest layer. This is known as reheating and occurs in all molten additive manufacturing processes. In steels, the martensite transformation starts at a certain temperature. For the tool steels studied, the start

temperature sits between 300 °C and 400 °C [33]–[35]. As the freshly deposited layer cools, the martensite transformation temperature is reached, causing the austenite to transform to martensite. Since the martensite finish temperature is below room temperature for H13 and Dievar, some austenite does not transform. This is known as retained austenite. The martensite finish temperature for QRO 90 is above room temperature, so retained austenite should not be present [35]. As the build increases in height, layers close to the deposition reach temperatures either above melting or below. Parts of the layers that do reach the melting temperature simply remelt and solidify with the latest deposition. Parts that do not reach the melting temperature but are heated to within the austenitizing temperature range experience austenitic transformation [25]. Parts that do not reach the austenitizing temperature range experience martensitic transformation and martensite tempering [25]. Even though the layers are not kept at temperature for a sufficient duration of time, some softening is expected. The last layers to be deposited are not reheated and do not undergo any martensite tempering. As a result, the hardness of the samples increases along the build direction.

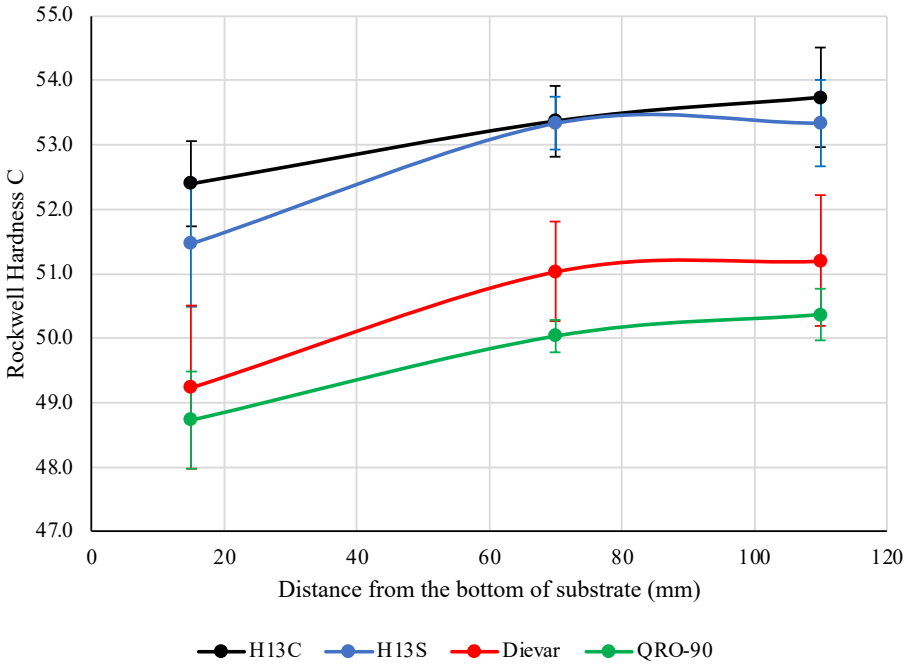

Figure 13: Rockwell Hardness Scale C measurements along the height of each sectioned specimen at 15 mm, 70 mm, and 110 mm from the substrate.

Upon sectioning the samples from Figure 12 large amounts of porosity were revealed at various locations in the build. Figure 14 displays these cross sections and the red circles highlight the defects found in the sample. Samples of H13 Cored and Dievar had defects as large as 2 mm in length, while samples of H13 Solid and QRO 90 both had a defect as large as 10 mm in length. Defects as large as these would be detrimental to the mechanical properties of the sample, so these samples were not machined into test coupons [42].

Figure 14: Cross sections of (a) H13 Cored, (b) H13 Solid, (c) Dievar, and (d) QRO 90 with red ovals showing large sized porosity at different locations in the builds.

Samples were further sectioned into 15 mm thick samples for metallographic inspection. Figure 15 shows the unetched optical micrographs from around 70 mm from the substrate in the as-built condition. All tool steels were produced with porosity and without cracks. In the sections analyzed, image analysis calculated that all the samples had relative densities higher than 99.5%. Porosity in WAAM is either categorized as raw-material induced or process-induced [43]. Spherical pores mainly originate from the wire feedstock and substrate plates. These surfaces can be contaminated due to improper handling. Moisture, grease, and other hydrocarbons can be easily absorbed into the molten pool and create gas bubbles that get trapped in the metal during solidification [44]. Cleaning the feedstock and substrate materials with acetone or surface grinding can mitigate the formation of these defects. Pores can also form due to the evaporation of high vaporization pressure elements [45]. Enforcing a dwell time between layers would allow for some of the gas pores to escape during solidification. Samples in Figure 15 (a) and (b) contain spherical pores. The wires and substrate were not cleaned prior to deposition so those spherical pores are a result of contamination. The pores in the H13 solid sample could also be formed from the evaporation of manganese. Irregularly shaped pores are processed-induced. If the power is not sufficient, incomplete melting or spattering may occur during deposition [46]. If not fully melted, the feedstock will not be able to fill the gaps between depositions, leaving behind large voids, known in AM as lack of fusion voids. Process-induced porosity can be remedied through adjustments in processing parameters to ensure complete melting or the reduction of space between deposition tracks. Figure 15(c) shows a lack of fusion void. Increasing the power used to melt the wire feedstock or reducing the distance between depositions would eliminate this defect.

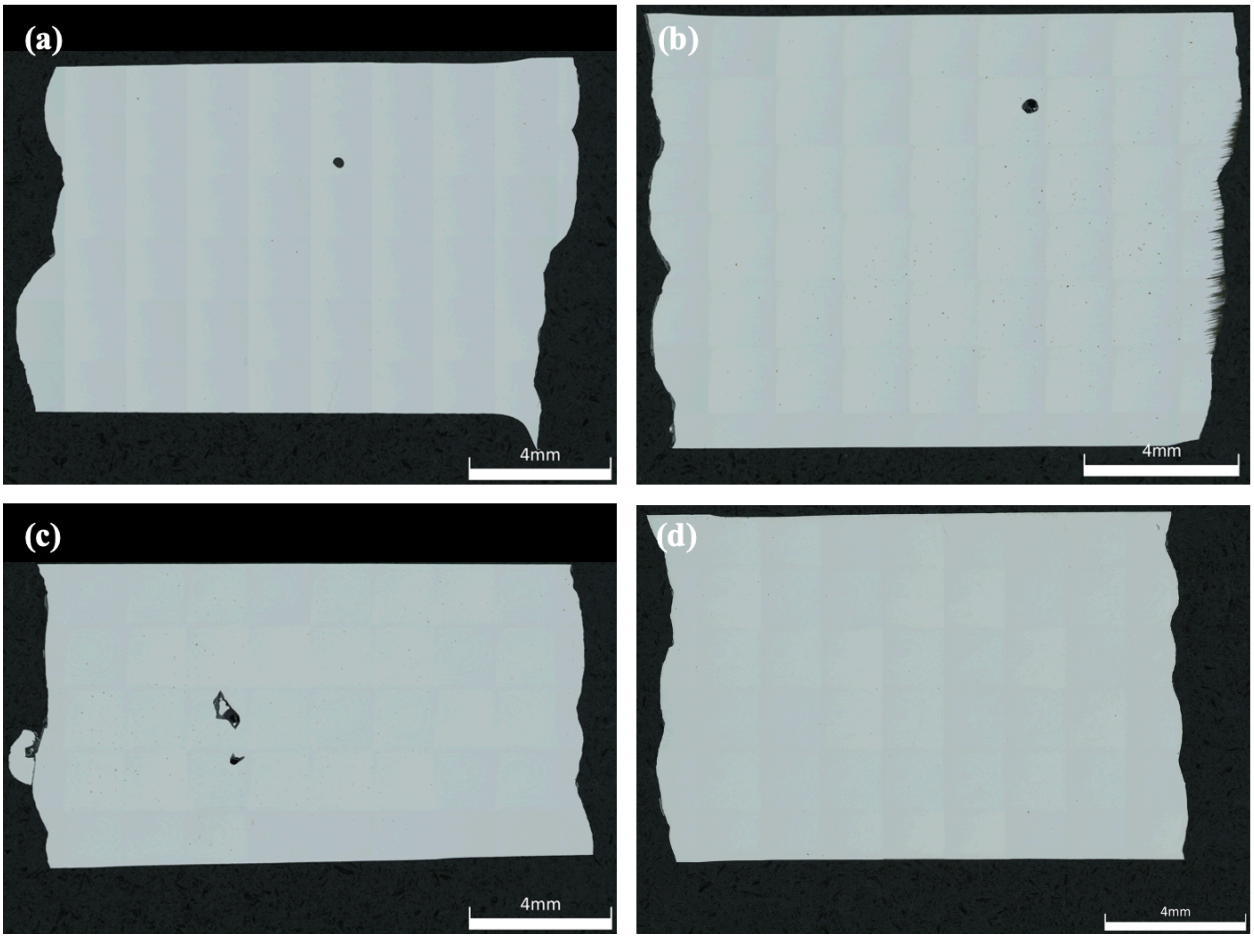

Figure 15: Stitched micrographs of the as-built condition (a) H13 Cored, (b) H13 Solid, (c) Dievar, and (d) QRO 90 in bright field.

Figure 16 displays the etched optical micrographs of the as-built samples in dark field imaging. Dark field imaging provided a better view of the grain structure. All four tool steels in the as-built condition possess large, vertically oriented columnar grains. Some of the columnar grains are millimeters in length. Coarse, columnar grains are typical in materials processed by AM [47]–[49]. During solidification, grains tend to grow epitaxially following the direction of the maximum temperature gradient formed from the welding torch [50]. Once formed, reheating of subsequent layers allows for these columnar grains to grow. Growth occurs along the <100> direction parallel to the local heat flow direction for cubic materials [51]. This results in the formation of large, vertically oriented columnar grains. The unidirectional orientation of the

grains results in anisotropic mechanical properties as observed by Wang et al. [24]. Anisotropic properties create complexity when it comes to part design. Each orientation must be tested and analyzed to provide engineers an understanding of whether the proposed design will survive expected load cases. Columnar grains are advantageous in parts like blades where unidirectional properties are desired. In most cases isotropic mechanical properties are desired to erase the complexity that arises from anisotropy.

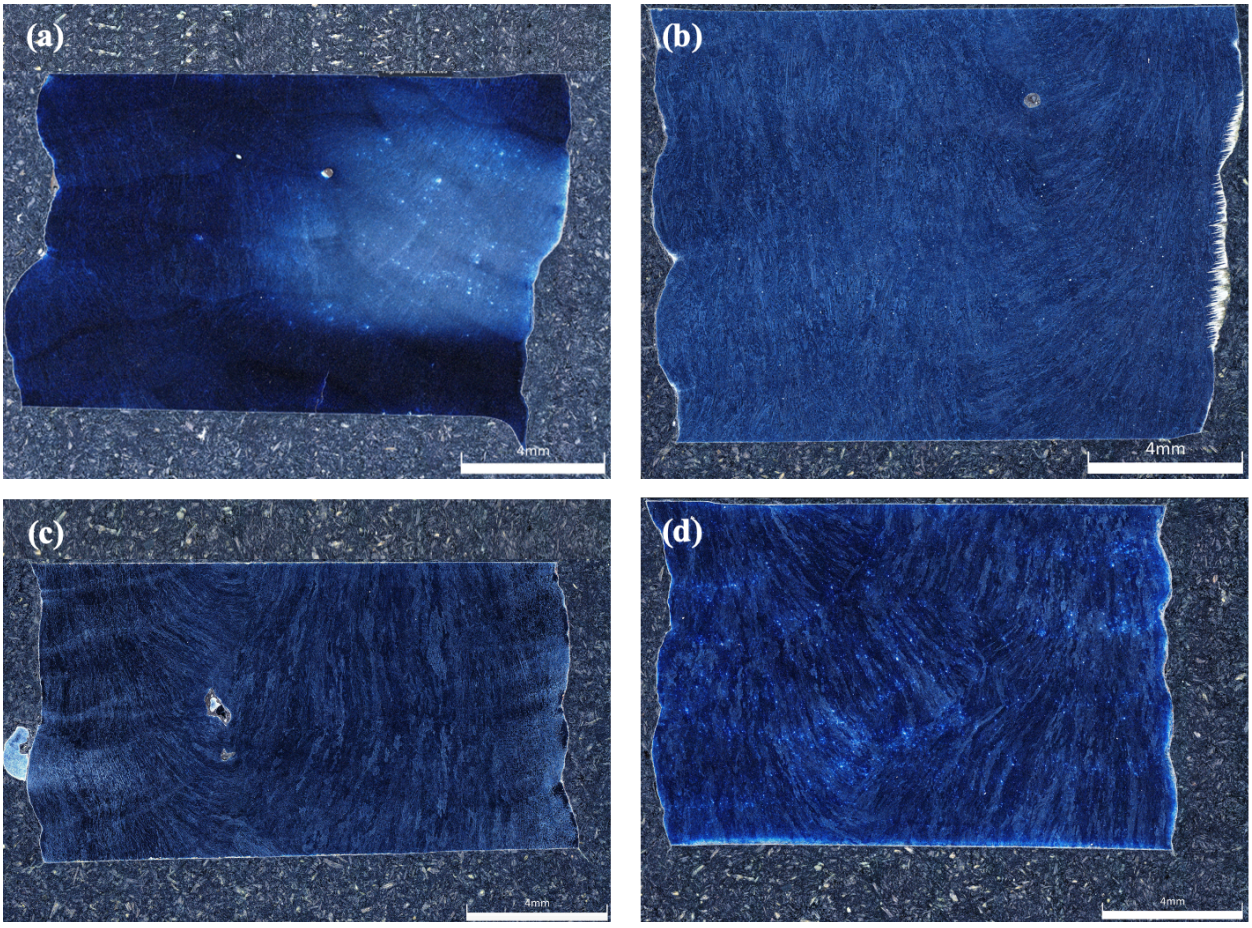

Figure 16: Stitched optical micrographs of etched H13 Cored, H13 Solid, Dievar, and QRO 90 taken in dark field.

Figure 17(a-d) display the microstructures of the etched samples at 2000X using differential interference contrast (DIC). DIC was used to further contrast the martensite and austenite. Figure 17(a) displays the microstructure of H13 cored. The phases visible under

optical microscopy are austenitic grain boundaries, tempered martensite, and ferrite. The tempered martensite is represented by the coarse laths. A group of needle-like martensitic laths that follow the same direction is called a martensitic lath packet [52]. The martensite packet is represented by the textured, elevated regions while the globular, shallow regions are ferrite. Since the examined sample was taken at the middle of the build height, the martensite was tempered due to exposure to high temperatures from remelting. Since the martensite finish temperature for H13 is below room temperature, retained austenite should be present in the microstructure. It is possible that the amount of retained austenite is too low to observed with optical microscopy as values below 15% are difficult to view with optical microscopy [53]. X-ray diffraction is commonly used to calculate the amount of retained austenite in ferrous metals with high accuracy.

The H13 solid sample in Figure 17(b) shows a network of smooth shallow regions. Tanvir et al. observes these features in their H13 samples processed by WAAM and verified this was austenite through energy dispersive spectroscopy (EDS) [28]. Furthermore, cast H13 tool steel possessed these same white networks after etching [45]. These smooth, shallow regions are white when imaged in bright field. These images are located in Appendix C. Thus, it can be reasonably assumed that these features in this work are retained austenite. The H13 solid wire contained more copper which stabilizes austenite. Thus, less austenite is transformed into martensite resulting in more retained austenite in the microstructure after cooling. The sample made of Dievar in Figure 17(c) had similar microstructure as the H13 solid sample. The Dievar wire feedstock was also copper coated so a similar fraction of retained austenite is to be expected. The QRO 90 sample had the least amount of retained austenite out of all four tool steels. Since the martensite finish temperature is above room temperature little retained austenite

should be present in the final microstructure. The globular shallow regions in Figure 17(d) may be ferrite.

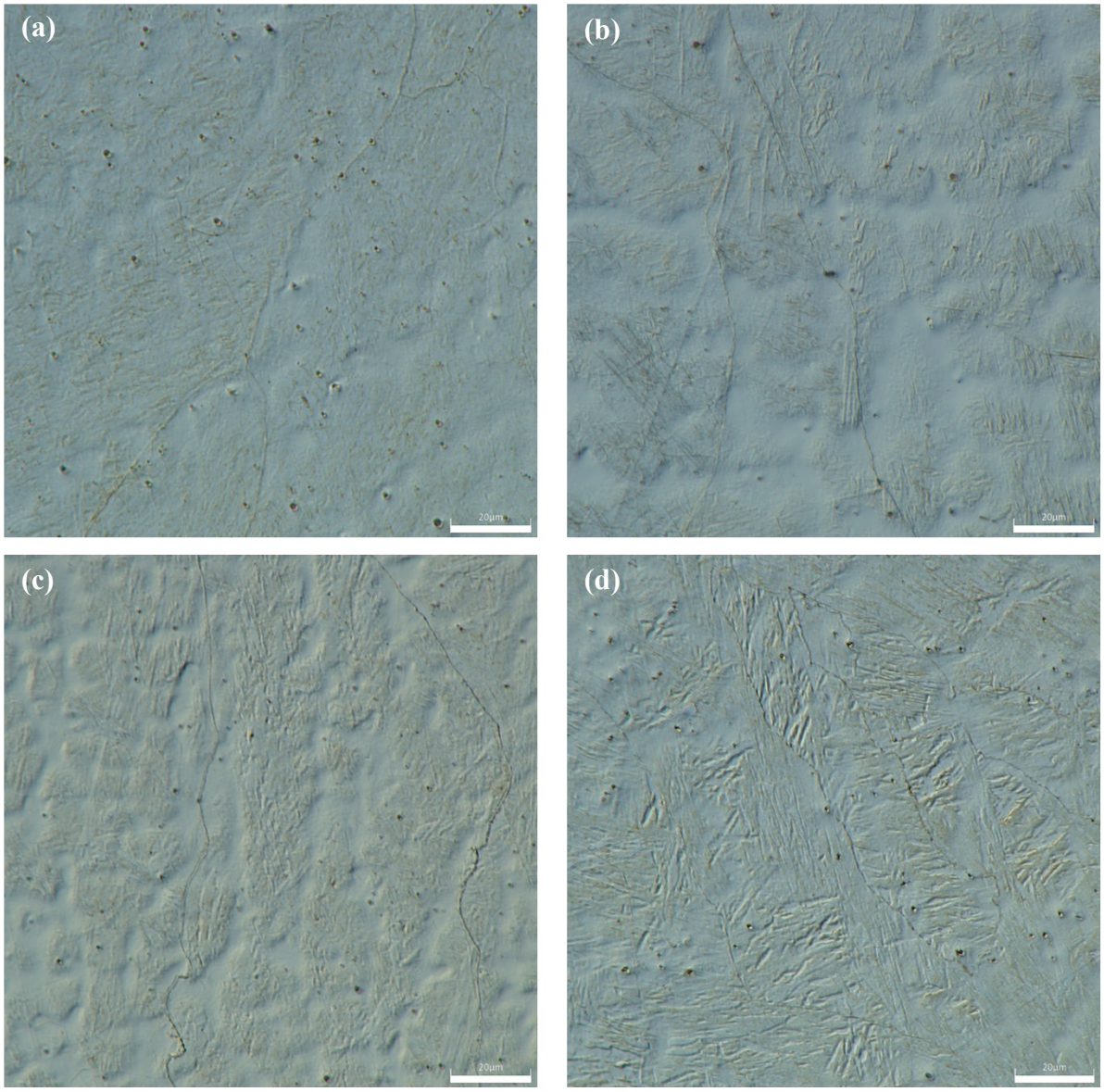

Figure 17: Optical micrographs using differential interference contrast of the microstructure of (a) H13 cored, (b) H13 solid, (c) Dievar, and (d) QRO 90 at 2000X. The scale bars on each image are 20µm in length.

Spherical particles are observed in all four feedstocks. It is important to distinguish whether these particles are carbides, pores, or a combination of both. Picral reagent outlines the carbides in tool steels [53]. As shown in the bright field images in Appendix C, the spherical

particles were not affected by the etching process. The samples etched sufficiently in Picral because of its success in etching the annealed microstructures that shown in the next section. It is believed that these observed spherical particles must be pores. Ge et al. characterized the porosity using X-ray computerized tomography and observed spherical gas pores sized as low as 2.8 μm [55]. Image analysis on the unetched images measured the sizes of the spherical particles and the measurements are displayed in Table 7. These particles are close to the diameters measured by Ge. From literature, the size of the carbides in additively manufactured tool steels are observed as small as 5 nm and as large as 100 nm [28], [55], [56]. Carbides have been observed to be rod like in shape with lengths as long as 225 nm [28]. The diameters measured in the current work are vastly different from those measured in literature. As a result, the spherical particles are likely gas pores.

Table 7: Average diameters of the spherical particles in the unetched micrographs of all four as-built microstructures.

	Average diameter (μm)
H13 Cored	1.861
H13 Solid	0.707
Dievar	0.982
QRO 90	1.115

Carbides should be present in all four microstructures. The most common carbides that exist in hot work chromium tool steels are MC, M_6C, M_7C_3, and $M_{23}C_6$ [57]. This distribution of each varies with chemical composition. As observed by Tanvir et al. and Huang et al. using scanning electron microscopy (SEM) the carbides are located on the ferrite, retained austenite, and along the austenitic grain boundaries [28], [54]. Visualizing and identifying each carbide is impossible without the aid of scanning electron microscopy and EDS. Understanding the differences in the distribution of carbides in all four microstructures would contribute to a total

understanding of how the microstructure is different from wrought and its response to heat treatments.

In summary, all four wire feedstocks were printed successfully without the presence of cracks. While the as-built condition of all four tool steels possessed porosity, process parameters can be adjusted and feedstocks can be properly prepared to eliminate these defects. Three-dimensional non-destructive testing such as computed tomography (CT) would provide a detailed understanding of the defects size, shape, and location for an entire part for a given parameter set. CT would be a more systematic method for detecting defects than cross sectioning, ensuring that an ideal processing parameter set would produce defect free parts. The high heat input generated by WAAM resulted in large, columnar grains for all four tool steels, signaling anisotropic mechanical properties. In addition, the high heat input also reheats previously deposited layers to temperatures in the tempering range, softening the martensite. As a result, the hardness of the sample decreases down towards the substrate. Along with softened martensite, the microstructure of all four feedstocks contains retained austenite, newly formed martensite, ferrite, and carbides. Copper was seen to promote the retention of austenite in H13 solid and Dievar microstructures. Its absence in the H13 cored microstructure promoted its transformation to martensite during remelting. QRO 90 has a martensite finish temperature above room temperature so despite its high copper content, most of the austenite was transformed to martensite upon quenching.

3.2 Comparison of the wrought and WAAM processed microstructure in the annealed condition

Tool steels are commonly hot worked to produce fine, equiaxed grains and then annealed to relieve stresses formed and soften the material [58]. Figure 18(a) displays the microstructure of wrought H13 sample in its as-received annealed condition. The grains are so fine that they

cannot be seen in the overview image. At 2000X the ferrite grains can be seen in Figure 18(b). These grains are microns in diameter and are equiaxed. The carbides and cementite are represented by the barely visible dots in the matrix. The soft ferrite matrix in the annealed state makes machining tool steels easier.

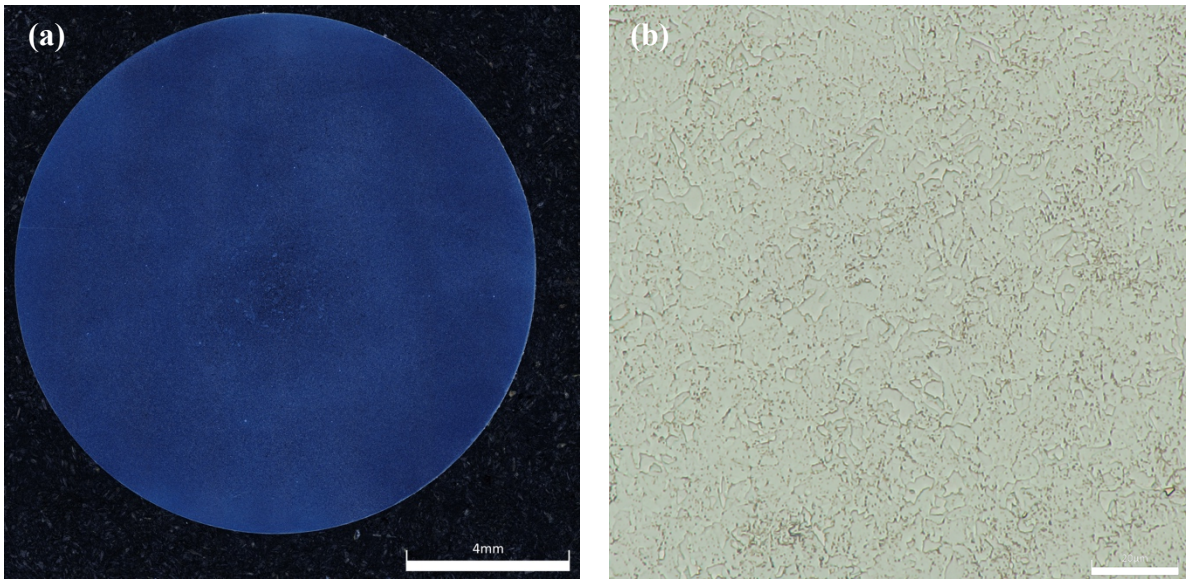

Figure 18: Micrographs of wrought annealed H13 (a) stitched overview image and (b) image at 2000X magnification in differential interference contrast to highlight ferrite grain structure.

Figure 19 displays the etched micrographs of all four tool steels after annealing heat treatment. It is apparent that the columnar grains are not eliminated after annealing. More energy to trigger recrystallization in the form of higher temperatures and/or soak times must be used to break down the columnar grains as demonstrated by Asala et al. [59].

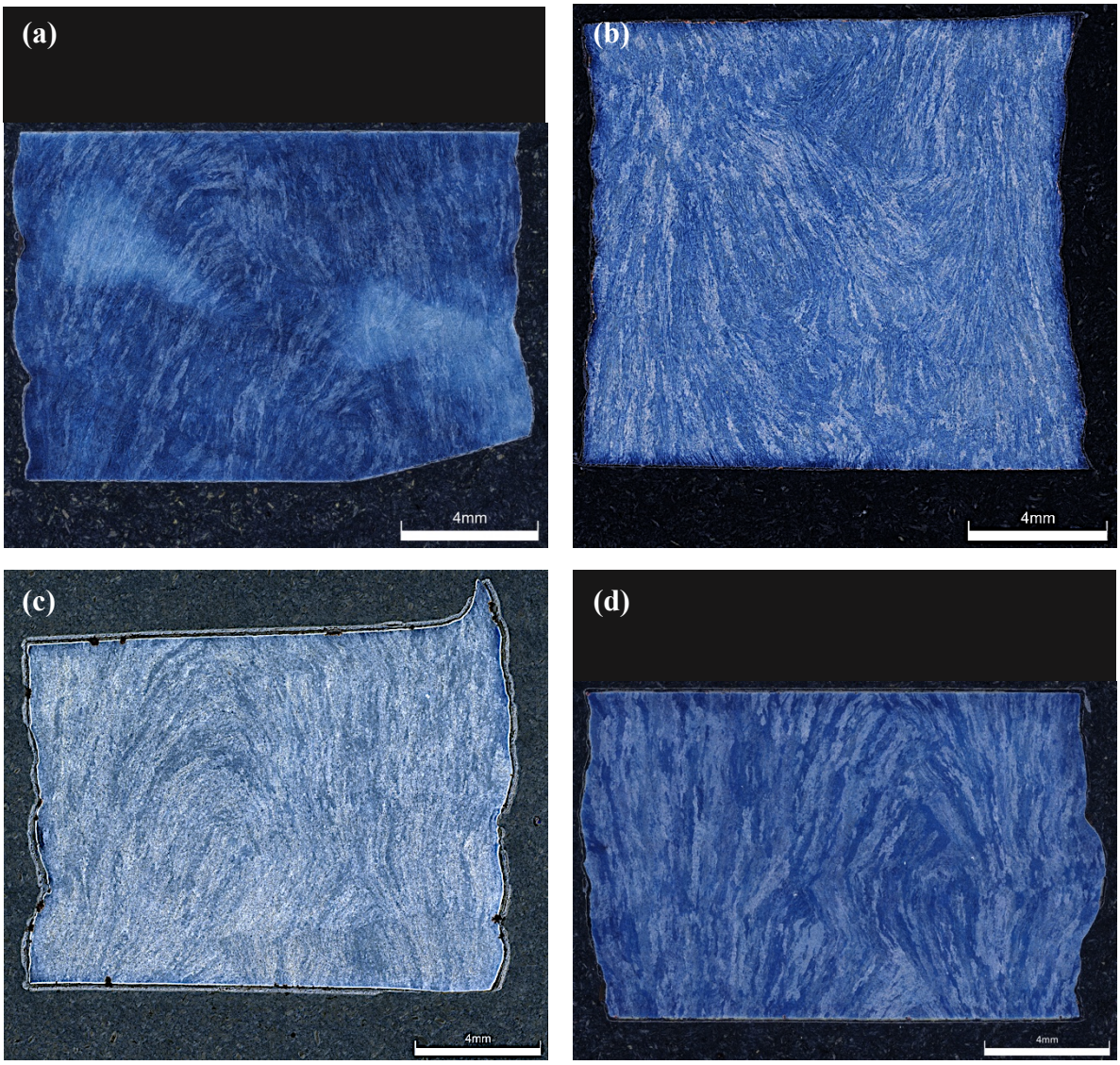

Figure 19: Stitched optical micrographs of etched annealed (a) H13 Cored, (b) H13 Solid, (c) Dievar, (d) and QRO 90 taken in dark field.

While the columnar grains did not change, the microstructural phases desired appeared in all four samples after annealing. The micrographs of all four feedstocks in Figure 20 display ferrite grains. The ferrite grains are slightly elongated and oriented with respect to the large columnar structures. Since recrystallization did not occur the grains keep their orientation which is parallel to the heat source during deposition. The carbides were prevalent in the H13 solid and Dievar sample and are represented by the dark circular outlines in between ferrite grains. The carbides are less distinguishable in the H13 cored and QRO 90 sample as they are represented by

the extremely fine dots in the microstructures. The carbides seen in the WAAM processed tool steels are all larger than the carbides seen in the wrought form. This is likely because of differences in starting microstructure prior to annealing. The hot-working procedure prior to annealing the wrought H13 sample must have produced carbides finer than those produced by WAAM. Distinguishing between alloy carbides and cementite is impossible using light microscopy; SEM would provide identification of the precipitates present in the microstructure. Hardness was measured on these annealed samples, but the values were very low that the machine could not measure the indents on the Rockwell C scale. Thus, hardness values are not displayed in this research for the annealed samples.

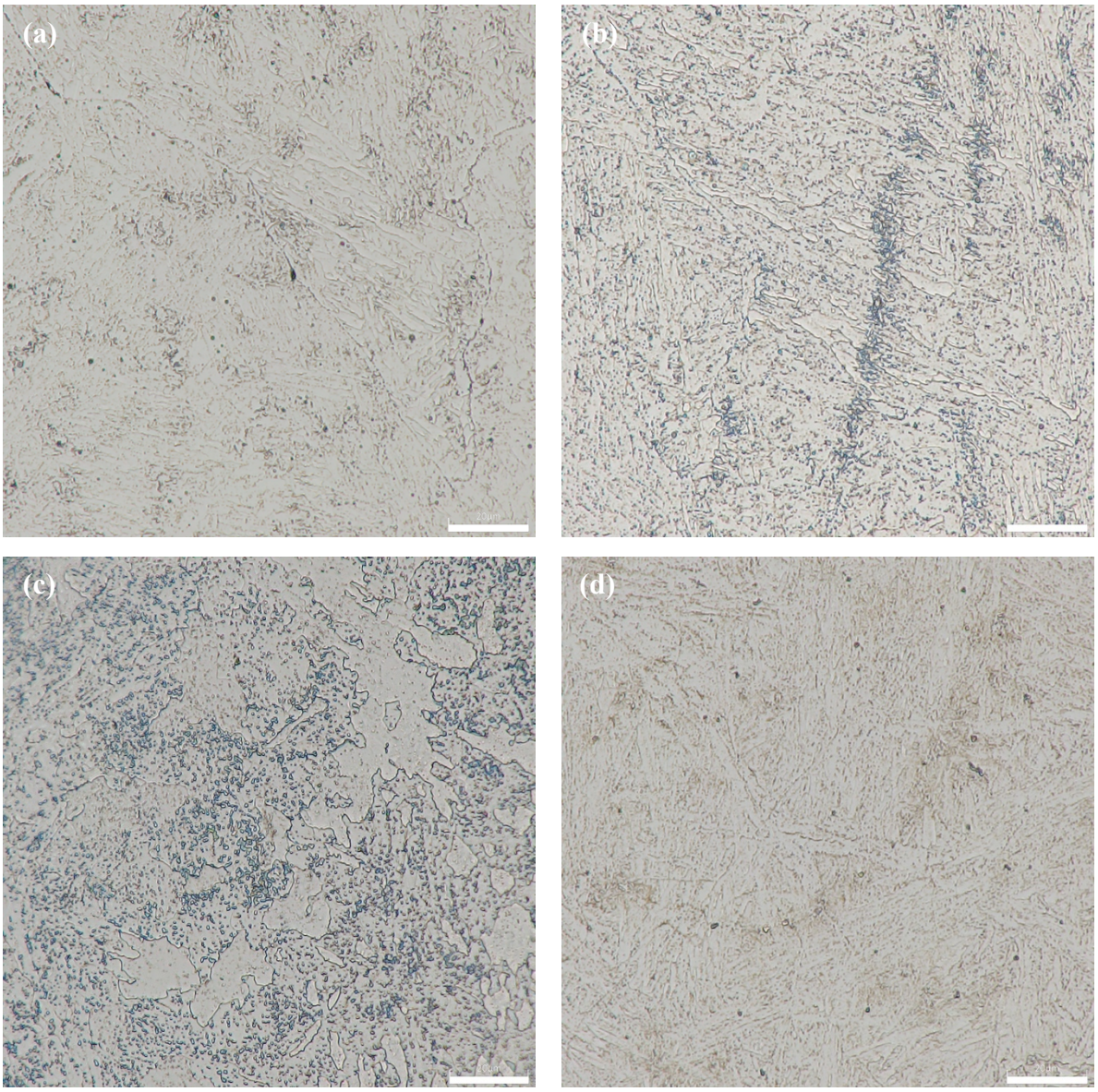

Figure 20: Bright field optical micrographs of the microstructure of (a) H13 cored, (b) H13 solid, (c) Dievar, and (d) QRO 90 at 2000X. The scale bars on each image are 20µm in length.

In summary, wrought H13 and tool steels processed by WAAM exhibit different grain structures. Wrought H13 has fine, equiaxed grains while H13 processed by WAAM has coarse, columnar grains. The annealing process did not transform the columnar grains to equiaxed grains because there was not enough energy to initiate recrystallization. Higher temperatures and soak times are required to transform the columnar grains in tool steels processed by WAAM. The carbide sizes in the WAAM processed tool steels appeared larger than that of the wrought H13

sample. This is likely due to differences in starting microstructure. While the grain structures and carbide sizes were different, the phases formed during the annealing procedure are similar for both the wrought and WAAM processed. The desired ferrite grains and carbides are observed in both the wrought and WAAM processed tool steel microstructures. As a result, the standard annealing procedure can be used on tool steels manufactured by WAAM.

3.3 The effect of increasing austenitizing temperature on hardness

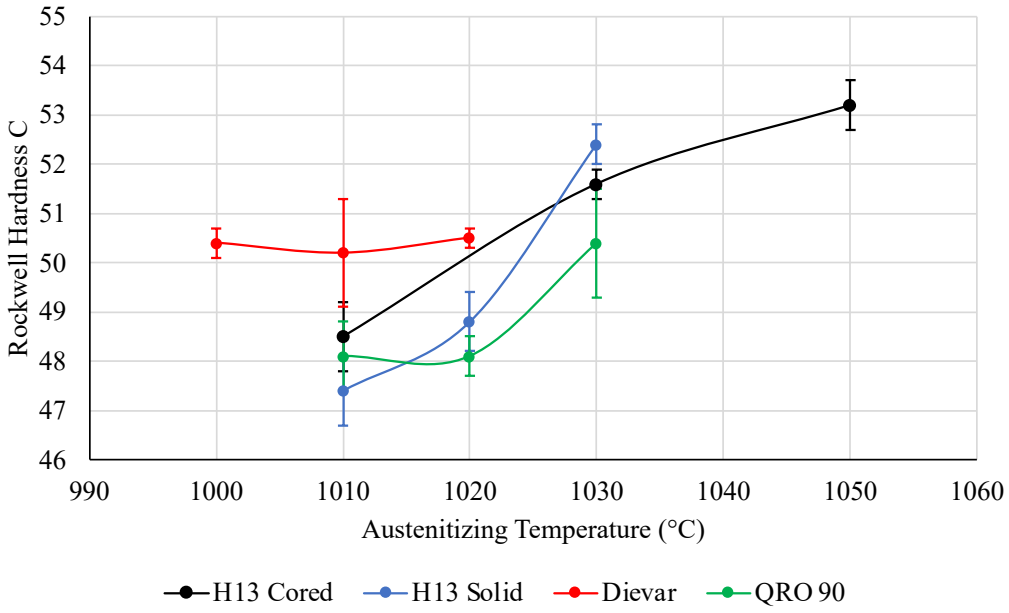

Figure 21: Rockwell hardness measurements at each austenitizing temperature for all four tool steel feedstocks.

Figure 21 displays the hardness measurements at austenitizing temperatures between 1000 °C and 1050 °C. For both H13 feedstocks, the hardness increased with increasing austenitizing temperature. This increase is likely due to strengthening of the martensite. When steel is heated into the austenite region, a fully austenitic matrix is formed. The carbides formed from annealing start to dissolve and carbon starts to diffuse into the austenite matrix [60]. During fast quenching the carbon rich austenite retains much of the carbon during martensitic transformation [61]. An increase in temperature would facilitate a faster dissolution rate of

carbides and a faster diffusion of carbon to the austenite since diffusion is driven by temperature [62]. Increasing carbon content in the martensite strengthens it [63]. Measuring the carbon content in the martensitic areas with EDS would validate if more carbon was present in the martensite at increasing austenitizing temperatures. Nanoindentation on the martensite packets for each austenitizing temperature would validate the strengthening of the martensite as a result of this increased carbon content. While the increased carbon content stabilizes the austenite against phase transformation, the increased amount of retained austenite is not large enough to significantly soften the matrix due to the low carbon content of H13 [64]. A change in the fraction of retained austenite was not seen in the microstructures for both H13 feedstocks in Figure 22. X-ray diffraction (XRD) would provide a quantitative insight on the evolution of retained austenite at increasing austenitizing temperatures. As a result, the higher austenitizing temperatures hardened both H13 feedstocks.

It was observed in Figure 21 that at 1010 °C, the H13 cored feedstock was harder than the H13 solid feedstock. The lower hardness of H13 solid feedstock is likely because of the increased copper content. Similarly, to how the as-built condition of H13 solid had more retained austenite than the H13 cored microstructure, copper stabilizes the austenite and slows the martensitic transformation during quenching from the heat-treatment [41]. At 1030 °C however, the H13 solid was harder than the H13 cored. This is likely due to grain growth in the H13 cored sample at this temperature. Copper in low carbon steels has been shown to refine the austenite grain size by enhanced solute drag [65]. Kang et al. saw grain refinement in high-carbon, high-chromium martensitic steels with increasing copper contents [41]. Because H13 solid has more copper than H13 cored, it is plausible that at this temperature the grains in H13 cored grew while

the grains in H13 solid did not grow. Finer grain sizes provide strengthening so the H13 solid would be harder than the H13 cored.

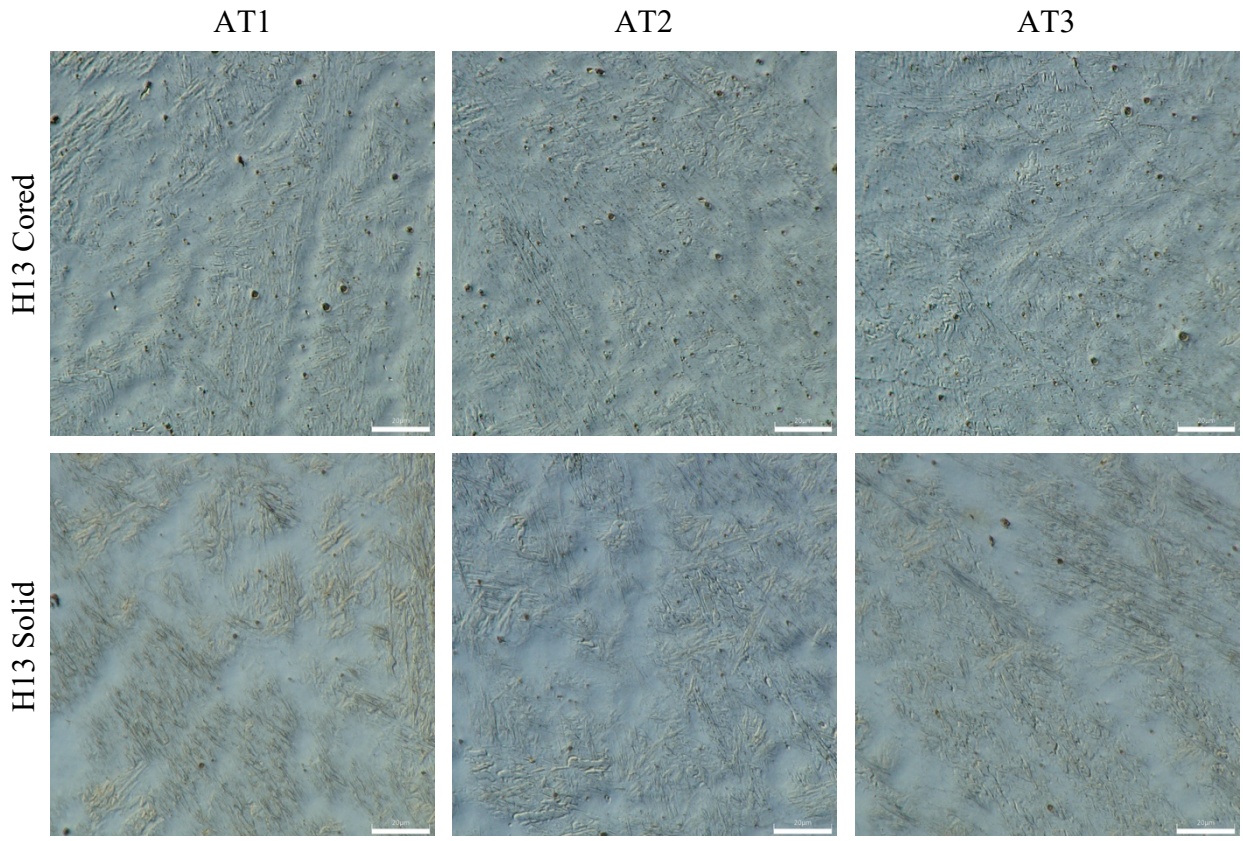

Figure 22: Microstructures of H13 Cored and H13 Solid at increasing austenitizing temperatures. The scale bars on each image are 20μm in length.

As observed in literature this trend of increased hardness with increasing temperature is not expected to maintain at higher austenitizing temperatures. At a certain high enough temperature, the carbides completely dissolve and the material will lose the strengthening effects from secondary hardening [66]. Furthermore, grain growth occurs at elevated temperatures. While the grains did not grow significantly with the austenitizing range tested, they are expected to grow at increased temperatures [63]. A complete dissolution of carbides and grain growth contribute to softening of the tool steel at elevated austenitizing temperatures. It is expected that a maximum hardness where the strengthening and softening mechanisms will reach equilibrium.

Looking at the hardness measurements from Dievar and QRO 90 in Figure 21 it appears that this maximum hardness was achieved. For Dievar the hardness plateaus between 1000 °C and 1020 °C while QRO 90 observed the same results between 1010 °C and 1020 °C. No obvious differences in martensite or retained austenite content were detected in Dievar and QRO 90 across all austenitizing temperatures as shown in Figure 23. In addition, both Dievar and QRO 90 feedstocks contain copper so theoretically grain growth should not occur [41]. This hardness plateau is most likely due to the behavior of the carbides at temperature. The Dievar and QRO 90 feedstocks have twice as much molybdenum than the H13 feedstocks. In tool steels, molybdenum reacts with carbon to form M_2C carbides [67]. These carbides dissolve at temperatures above 750 °C and react with iron to form M_6C carbides [67]. M_6C carbides dissolve at temperatures above 1150 °C and have dissolution rates that are slower than the other metal carbides like $M_{23}C_6$ [68]. With increased molybdenum contents, Dievar and QRO 90 should have a larger distribution of M_2C and thus, more M_6C carbides during austenitizing. The temperatures used for Dievar and QRO 90 are lower than the M_6C dissolution temperature, so the M_6C carbides should not dissolve. If the carbide dissolution is low, the amount of dissolved carbon present in the austenite should remain relatively constant. The carbon content in the martensite then should remain constant at increasing temperatures. As a result, the martensite should not strengthen as seen in the hardness measurements from Dievar and QRO 90. SEM and EDS would be needed to image and identify the carbides to compare their sizes at increasing temperatures and compare the M_6C distribution with the H13 feedstock.

Since the hardness values measured for QRO 90 were lower than that of the as-built, an alternative quenching media was used. A sample of QRO 90 was heated to 1030 °C and then quenched with forced air. Forced air was used to accelerate the cooling rate. A faster cooling rate

results in stronger martensite as less carbon is allowed to escape the austenite so more carbon remains in the lattice structure as it transforms to the BCT martensite structure [69]. Quenching in forced air resulted in an increase in hardness close to the as-built hardness. Comparing the carbon contents in formed martensite during still air quenching and forced air quenching would validate this result. The cooling rate needs to be measured so that it may be replicated when quenching larger sized QRO 90 parts.

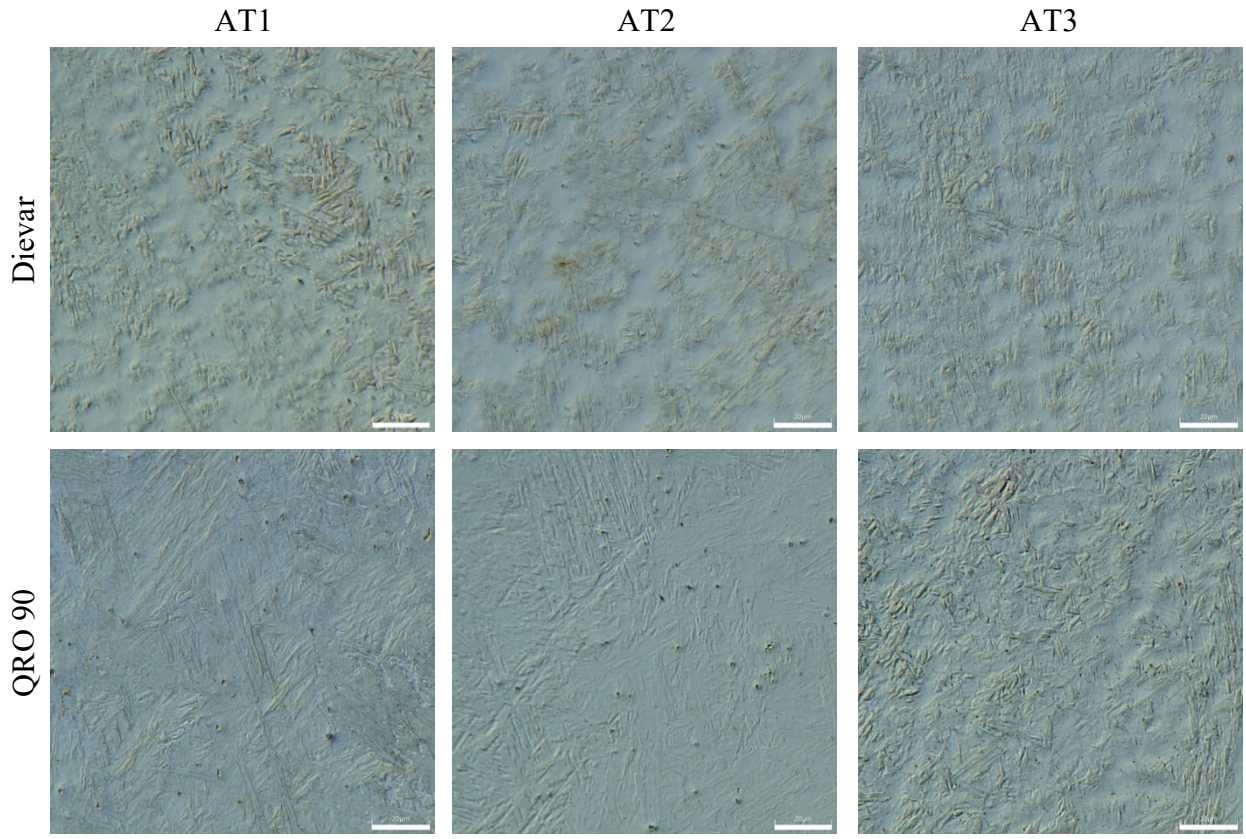

Figure 23: Microstructures of Dievar and QRO 90 at increasing austenitizing temperatures. QRO 90 at AT3 was heated to 1030 °C, but quenched in forced air to promote martensite transformation. The scale bars on each image are 20µm in length.

3.4 Comparison of the microstructures from the as-built and the austenitized condition

Even though austenitizing has demonstrated the ability to reach the same measured hardness as the as-built condition, the microstructures are different. This is expected as both conditions have different thermal histories. To understand how these differences result in similar

hardness measurements the quenched microstructure must be analyzed and compared to the as-built condition. As mentioned in section 3.1, the as-built microstructure consists of martensite, tempered martensite, retained austenite, fine carbides, and ferrite.

Looking at the austenitized microstructures in Figure 24, the quenched martensite appears finer than the as-built condition, indicating that these are un-tempered. Tempered martensite is not expected after this heat treatment cycle since the newly formed martensite is not reheated after quenching like in the as-built condition. The H13 solid and Dievar samples have the same smooth network regions as the as-built condition. Surprisingly enough, the austenitized QRO 90 looks to have these same features as well. This is expected since all three feedstocks contain copper which stabilizes austenite. Optically, the amount of retained austenite in austenitized H13 solid and Dievar look similar to their as-built conditions. A more quantitative comparison of the retained austenite should be done with XRD measurements in order to make a conclusion. QRO 90 in the austenitized condition has more retained austenite than its as-built condition. This difference is likely attributed to the differences in thermal history. The heat-treated samples are removed from the furnace and cooled uniformly to room temperature. However, during additive manufacturing the retained austenite is reheated to high enough temperatures to cause martensitic transformation. Since the heat-treated QRO 90 was not reheated after quenching it should contain more retained austenite than its as-built condition.

It is difficult to compare the H13 cored sample due to large fraction of porosity in both samples, but it is likely that the austenitized sample has more retained austenite than the as-built for reasons similar to QRO 90. While not visible with optical microscopy, the size of the carbides in both microstructures must differ. The as-built condition has a distribution of fine cementite and carbides. During annealing the M_2C carbides dissolve to form M_6C, while

cementite and the other carbides grow. As previously mentioned the M_2C carbides dissolve to form M_6C carbides [67]. During austenitizing, the remaining M_7C_3 and $M_{23}C_6$ carbides start to dissolve. Complete dissolution is not expected until 1100 °C for these carbides [70]. The M_6C and MC carbides may grow as their dissolution temperature exceeds 1100 °C; the temperatures used for austenitizing do not exceed 1050 °C in this work[67], [71]. The M_6C and MC carbides after quenching are larger than the sizes of the carbides in the as-built condition. The degree of dissolution of the M_7C_3 and $M_{23}C_6$ carbides is unknown so they could be larger or smaller than their sizes in the as-built state.

It is likely that the matching hardness values of the as-built and austenitized condition are a result of differing, but equal in magnitude strengthening and softening mechanisms. It is possible that the strengthening from martensite formation during austenitizing is equivalent to the secondary hardening from the fine carbides in the as-built condition. It is also possible that the softening from the larger carbide size after austenitizing is equivalent to the softening from martensite tempering. This would explain how equivalent hardness values can be achieved with differing microstructures in tool steels. An in-depth characterization of the carbide sizes with SEM is required to verify these points.

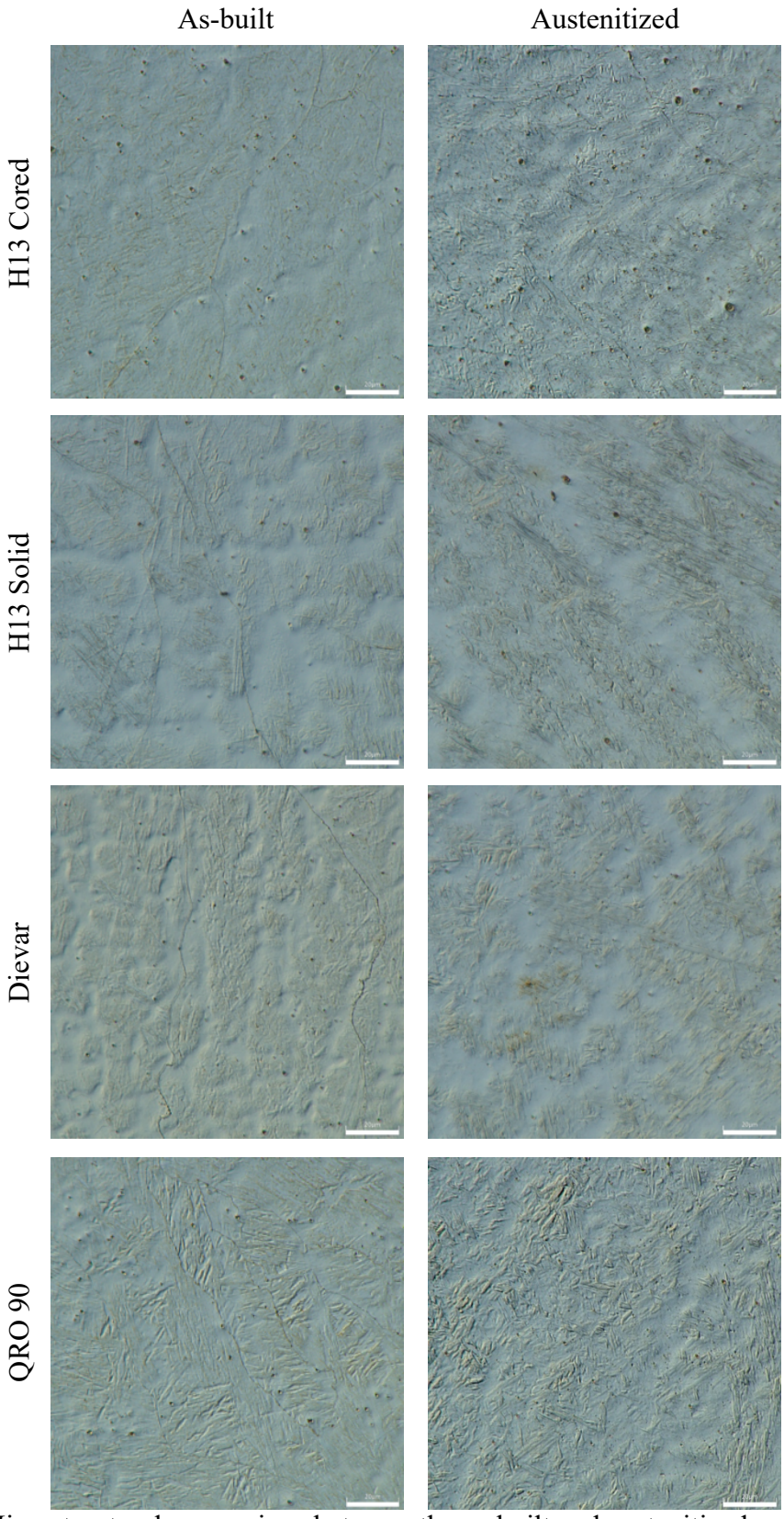

Figure 24: Microstructural comparison between the as-built and austenitized condition with equivalent hardness values. The scale bars on each image are 20μm in length.

The wrought H13 sample was austenitized under the same conditions as the H13 solid sample. The wrought H13 sample had a hardness of 55 HRC which is slightly harder than that of the hardened WAAM processed sample. Since the quenching conditions were the same, the discrepancy in hardness must be due to the differences in grain size. Figure 25(a-b) displays the microstructure of hardened wrought H13 and hardened WAAM processed H13. After austenitizing the grains in the WAAM processed H13 remains large, columnar while the grains in the wrought form are too fine to see at this magnification. Figure 25(c) shows a magnified view of the wrought microstructure where the fine grains are revealed. While an accurate measurement of the grain size was not done, it can be seen that the WAAM processed grains millimeters in size while the wrought grains are micrometers in size. Finer grain sizes typically result in higher hardness values [72]. Thus, the wrought H13 sample is harder than the WAAM processed H13 sample due to its fine grains.

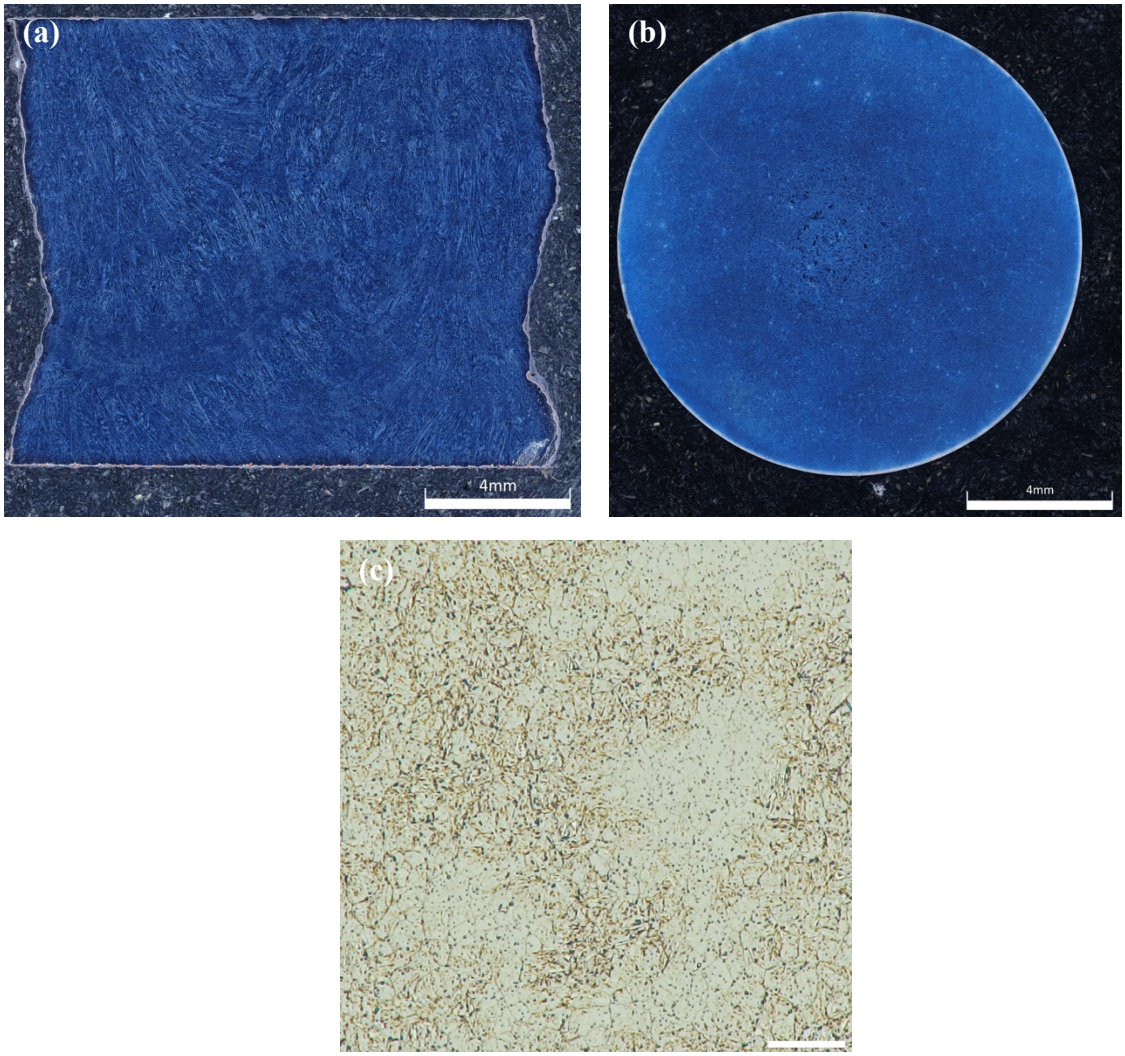

Figure 25: Images of the austenitized microstructures of the (a) WAAM processed H13, (b) wrought H13, (c) wrought H13 viewed at 2000X in bright field imaging. The scale bar in (c) is 20μm in length.

In summary, it was demonstrated that annealed WAAM processed tool steels can be hardened back to their as-built hardness. Two trends were observed with increasing austenitizing temperature. The H13 feedstocks observed an increase in hardness with increasing temperature, due to the strengthening of martensite. The Dievar and QRO 90 observed no change in hardness with increasing temperature as the martensite was not strengthened as a result of the decreased dissolution of carbides during austenitizing. While increasing temperature did not increase the hardness for QRO 90, increasing the quench rate was successful. The microstructures of the

austenitized WAAM processed tool steels consisted of un-tempered martensite, ferrite, retained austenite, and carbides. The austenitized microstructures consisted of a smaller fraction of retained austenite, ferrite, and larger carbides than the as-built microstructure. Different thermal histories caused this difference in microstructures. When comparing the WAAM processed H13 with wrought H13 under the same heat-treatment conditions, wrought H13 was harder due to its finer grain size.

3.5 The effect of tempering temperature on the hardness of conventionally heat-treated samples

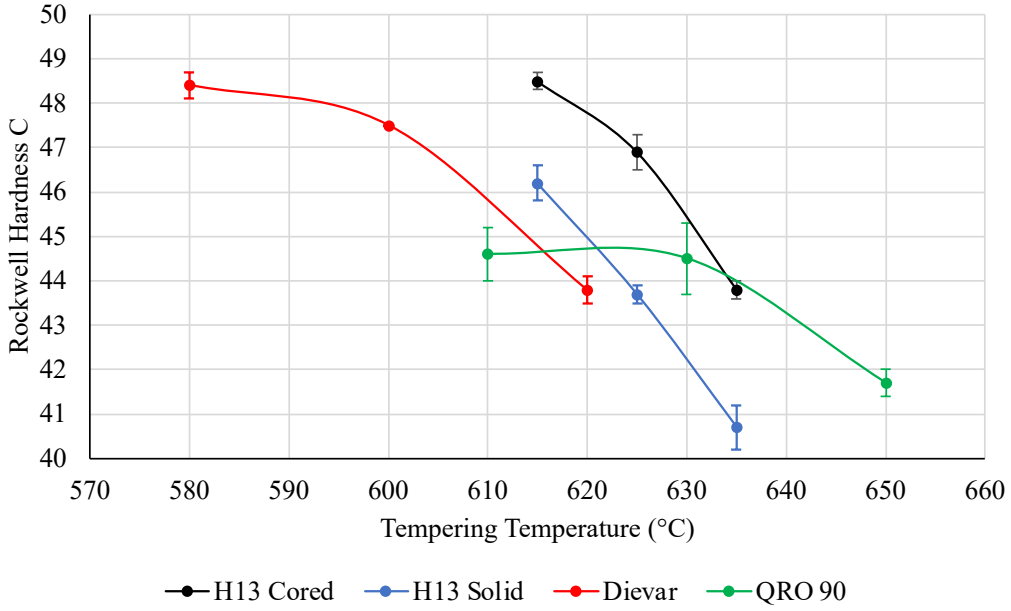

Figure 26: Rockwell hardness measurements at each tempering temperature after austenitizing for all four tool steel feedstocks.

Figure 26 displays the hardness measurements at each tempering temperature. It is shown that tempering WAAM processed tool steels was able to soften the material down to the desirable hardness range of 44 to 48 HRC. This was expected since at temperature, carbon diffuses out from the martensite structure to form ferrite, cementite, and alloy carbides [62]. Dislocations induced from the martensite transformation are also annihilated, reducing the hardness [73]. Each tool steel saw a decrease in hardness as temperatures increased. This can be

explained with the concept of diffusion. Since diffusion is driven heavily by temperature, diffusion occurs rapidly at higher temperatures [62]. Increasing temperatures accelerates carbon diffusion out of the martensite, providing more carbon atoms to the carbides promoting growth [63]. Less carbon in the martensite decreases its strength [74]. As a result, the coarsening of carbides indicates weakening of the martensitic structure. The presence of carbides large enough to observe can be seen in Figure 27. In tempered microstructures the carbides form in between martensitic laths and along grain boundaries [75]. After all the tempering trials for H13 solid and QRO 90, the carbides are represented as the brown-colored regions in the tempered martensitic regions and along grain boundaries in Figure 27. The carbides in these two feedstocks are visible because they have coarsened to a size observable with light microscopy. The brown-colored regions grow larger with increasing temperature as well. The carbides in H13 cored and Dievar are not visible because they might still be small and not observable with light microscopy. SEM would provide details on the size of these carbides. With large carbides it is expected that the H13 solid and QRO 90 would have low hardness values. As shown in Figure 26, H13 solid and QRO 90 have lower hardness values than H13 cored and Dievar. The difference in carbide size also explains why H13 cored is harder than H13 solid after identical tempering treatments. In order for H13 cored and Dievar to reach the same hardness values, temperatures for tempering have to increase to grow the carbides. As a result, an increase in temperature produces a weaker martensite, larger carbides and a lower hardness value.

Since the martensite start temperature sits around 300 °C, retained austenite transforms to martensite upon quenching from tempering. Thus, the tempered microstructure should have a significantly reduced amount of retained austenite. The microstructures for each tool steel at each tempering temperature is displayed in Figure 27. As shown the smooth network-like features are

absent from all the tool steel microstructures, suggesting a significantly reduced amount of retained austenite. As previously mentioned, retained austenite under 15 percent is difficult to view with optical microscopy, so it can be concluded that all four feedstocks after tempering have less than 15% retained austenite. XRD would provide quantitative results on the retained austenite content after tempering. Although martensite formed during quenching, the strengthening from martensite transformation is outweighed by the tempered martensite and coarsened carbides. The fraction of retained austenite present after hardening is very low compared to the fraction of martensite. A low fraction of martensite will be formed during quenching compared to the large fraction of the matrix that was softened during tempering. Thus, all four tool steel feedstocks experienced softening after tempering.

Some of the microstructures in Figure 27 have porosity. These pores are not a result of heat treatment. Since the process parameters have not been optimized and the feedstock not thoroughly cleaned, the as-built samples are expected to have gas porosity.

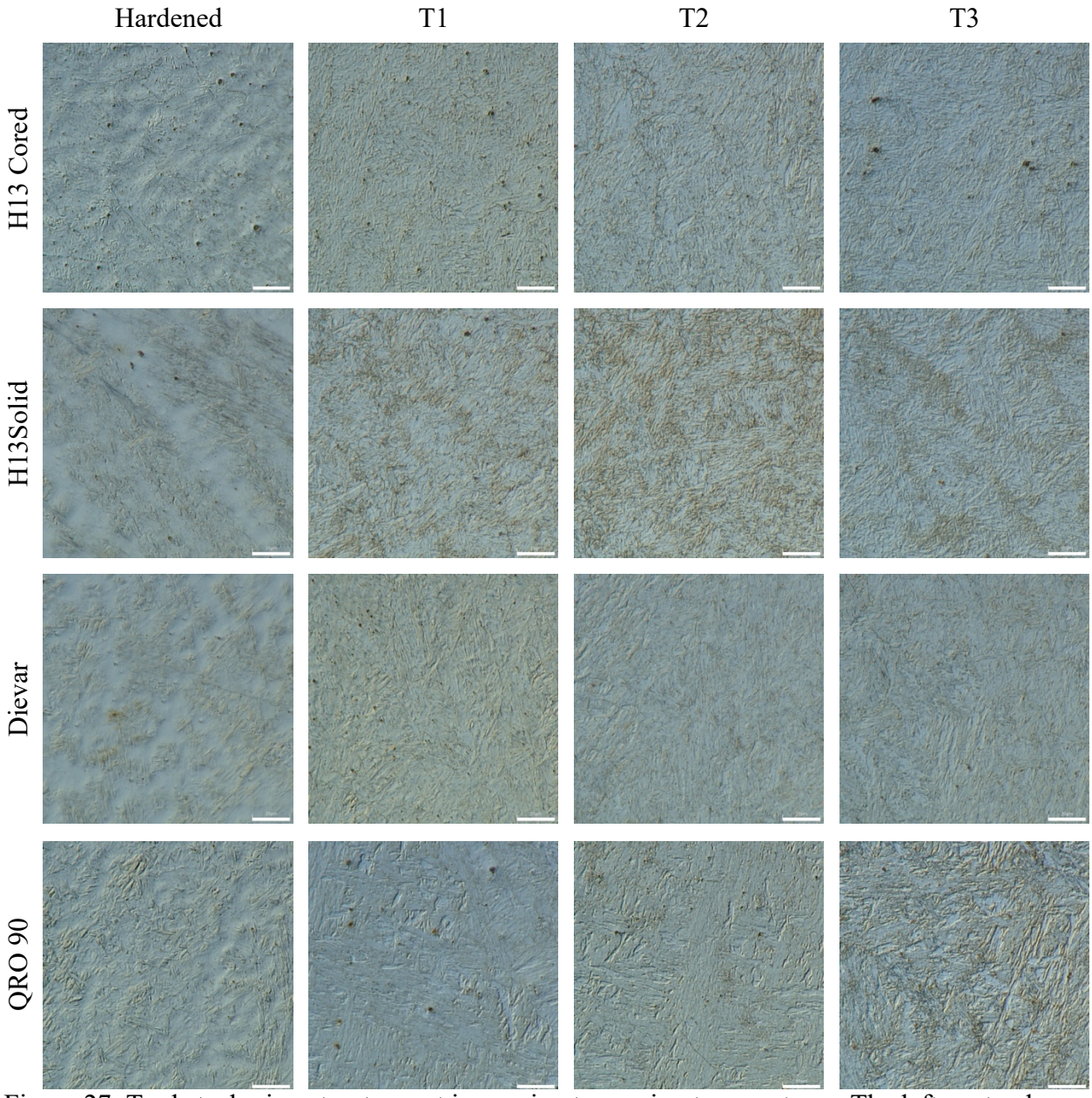

Figure 27: Tool steel microstructures at increasing tempering temperatures. The leftmost column shows the microstructure in the as-built state. The scale bars on each image are 20μm in length.

3.6 The effect of tempering temperature on the hardness of samples in the as-built condition

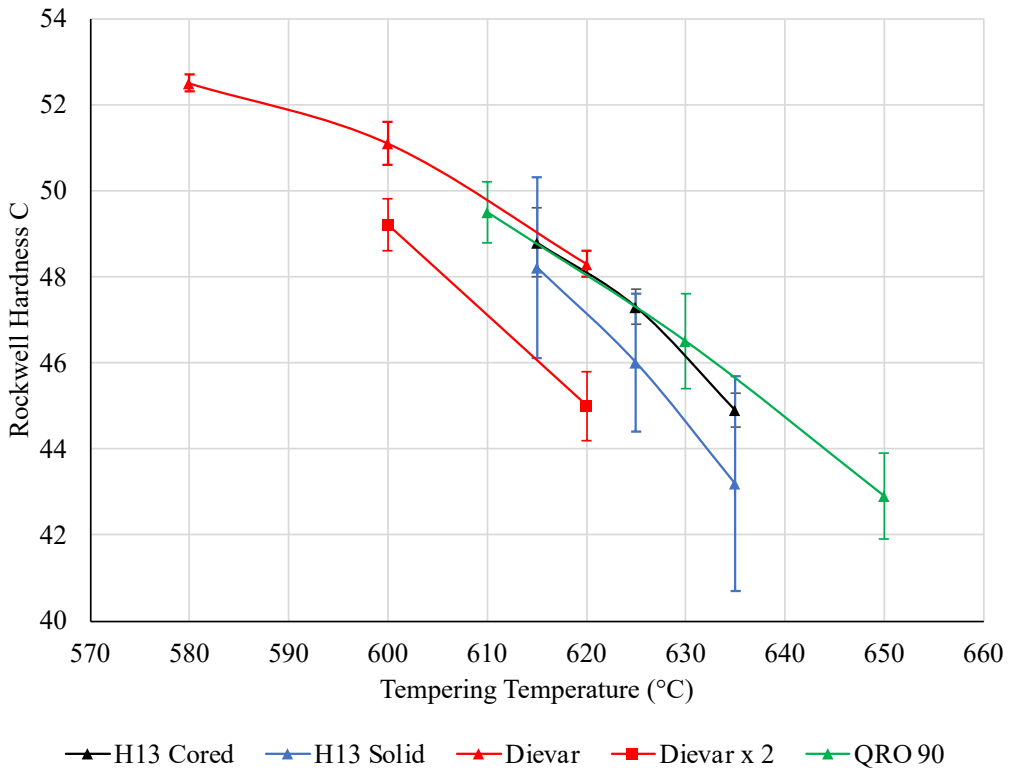

Figure 28: Rockwell hardness measurements at each tempering temperature when taken directly from the as-built state for all four tool steel feedstocks.

Figure 28 displays the hardness measurements at each tempering temperature. Similar to the conventionally heat-treated samples, tempering directly from the as-built state can soften the material down to the desirable hardness range of 44 to 48 HRC. Softening occurs because of the diffusion of carbon from the tempered martensite to the fine carbides, coarsening them [75]. Residual stresses that formed during the deposition process may have also been relieved while tempering [40]. The hardness decreased with increasing temperature much like the conventionally heat-treated samples. The discussion of temperature's impact on the rate of carbon diffusion in the previous section applies to this trend as well. SEM and EDS of the martensite and carbides would help to verify the distribution of carbon in martensite and coarsening of the carbides. Since the as-built condition has retained austenite, martensitic

transformation upon quenching is expected. Like the conventionally heat-treated samples, the smooth network like structures in the as-built state are also absent after each tempering trial as shown in Figure 29. With the absence of these features, the retained austenite content must be less than 15%. Further analysis with XRD would provide a quantitative measurement of the retained austenite content. The directly tempered microstructures exhibit the same coarsening of carbides in the H13 solid and QRO 90 samples. The carbides are the brown-colored regions in between the martensitic laths and along grain boundaries. Similarly, increased tempering temperature resulted in larger carbides in both feedstocks. Hardness measurements decreased as the carbide regions became more visible. Because of this it is fair to assume the decrease in hardness for H13 cored and Dievar feedstocks are a result of coarsening carbides. The carbides are still fine enough to where they are not observable with optical microscopy, but SEM would be used to understand the sizes of them.

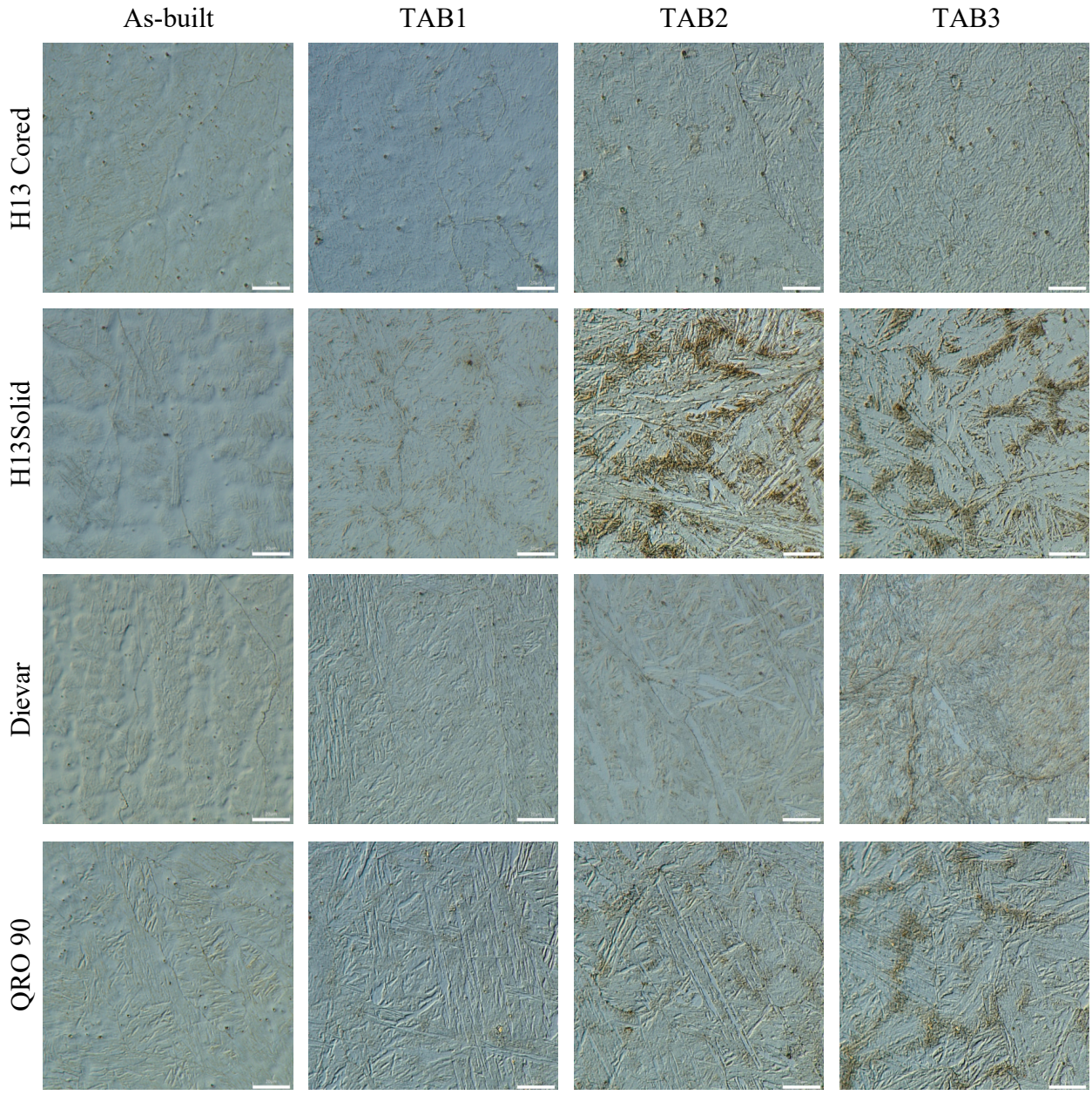

Figure 29: Microstructures of tool steel feedstock that were tempered from the as-built state. The leftmost column shows the microstructure in the as-built state. The scale bars on each image are 20μm in length.

While both H13 feedstocks and QRO 90 softened as expected during tempering, as-built Dievar strengthened during tempering at 580 °C and 600 °C. For reference, the as-built hardness was 50 HRC. This strengthening may be attributed to martensitic transformation upon quenching from heat-treatment. However, the H13 solid and Dievar as-built microstructures similar

contents of retained austenite, so it may not be from the strengthening from martensite formation. It has been shown that the tempering response is dominated by strengthening due to martensitic transformation rather than softening in steels with high copper contents [41]. However, this strengthening was only observed when tempering Dievar directly from the as-built condition. Both the H13 solid and QRO 90 samples softened after tempering. Furthermore, the H13 solid and Dievar as-built microstructures while had differing copper contents, but similar contents of retained austenite, so strengthening from martensite formation does not seem to be the cause.

A look into the differences in chemical composition might shed light on this observation. Since H13 and Dievar have different molybdenum and silicon contents, the type and size of carbides formed is expected to be different. Molybdenum in tool steels tends to form M_2C carbides and silicon promotes the formation of M_6C carbides [67]. With double the amount of Mo and significantly less silicon in Dievar than H13, it is possible that more M_2C carbides precipitated out in Dievar during tempering compared to M_6C carbides. M_2C carbides are harder than M_6C carbides, which may suggest why Dievar experienced hardening after tempering as opposed to the other feedstocks [57]. Understanding the size and distribution of these carbides in SEM or TEM would further support this explanation.

In an attempt to soften as-built Dievar to the desirable hardness range, the as-built sample was subjected two tempering cycles at 600 °C and 620 °C. As shown in Figure 28, the second tempering cycle softened Dievar to the desirable hardness range. During the second tempering cycle, the martensite formed from the first temper softened due to carbon diffusion and growth of carbides. The microstructures of Dievar from each tempering cycle is shown in Figure 30. The carbide regions are larger to a point where they can be observed with light microscopy at each

temperature after a secondary temper. Therefore, taking as-built Dievar through a secondary temper caused the carbides to coarsen significantly, resulting in the lower hardness values.

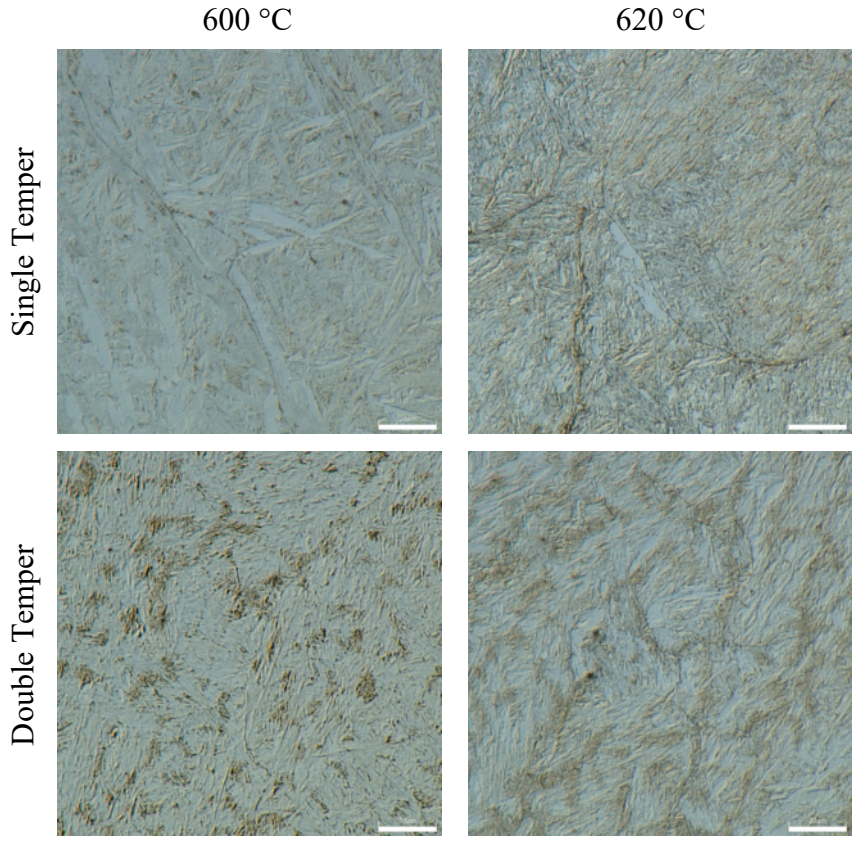

Figure 30: Microstructural comparison between a single and double temper on WAAM processed Dievar at 600 °C and 620 °C. The scale bars on each image are 20µm in length.

3.6 Comparison of the conventional heat treatment cycle and the directly tempered cycle

It can be inferred from Figure 26 and Figure 28 that the tempering responses of the austenitized and the directly tempered samples differed. The deviation of hardness measurements at each temperature for the conventionally heat-treated tool steels was much lower than that of the directly tempered. This can be attributed to the uniform microstructure of ferrite and carbides produced from annealing. Subsequent heat-treatments will yield a uniform as a result. In the as-built condition, the microstructure is non-uniform. Due to remelting, the microstructure can vary along the height of the build. As a result, the hardness will vary slightly.

The average hardness values for the directly tempered samples were higher than those for the conventionally heat-treated samples. This is likely due to the difference in size of the carbides prior to tempering. Up to a certain size, the carbides in tool steels are coherent with the matrix [76]–[78]. After this critical size, the carbides lose coherency with the matrix and decrease the effect of secondary hardening [79]. Since the austenitized carbides are thought to be larger than the as-built carbides, tempering would only further grow the remaining M_7C3, $M_{23}C_6$, MC, and M_6C carbides, making them more incoherent with the matrix. As a result, the carbides after a conventional heat treatment are larger than those after a direct temper and contribute to this difference in hardness. The fact that the tempering response between the conventionally treated and directly tempered Dievar differed weakens the argument that the differences in initial retained austenite content caused this difference in hardness after tempering. It is possible that carbides in the as-built Dievar condition grew to the critical size after a single temper at 580 °C and 600 °C and then lost coherency at 620 °C. Understanding the evolution of carbide size during heat-treatment with SEM or TEM is necessary to further these claims.

The wrought H13 sample was austenitized at 1030 °C and tempered at 615 °C for two hours so that a direct comparison can be made to the WAAM processed H13 solid sample. Figure 31 showcases the resulting microstructure in DIC. The prior austenite grain boundaries appear to have a brown color which was assumed to be a chain of carbides. Visible carbide regions and small ferritic regions indicates a soft matrix. The measured hardness for this sample was 44 HRC which is softer than the WAAM processed H13 after conventional heat treatment and direct temper. When comparing the microstructures, the wrought H13 had coarser carbides and more ferrite. It is likely that due to the fine grains, the carbon atoms travel a shorter distance to the grain boundaries where carbides remain after tempering [75]. A decrease in distance

would increase the concentration gradient between the carbides in the grain boundaries and the carbon in the martensite. The concentration gradient is the driving force for diffusion so at this temperature diffusion occurred sooner than the WAAM samples resulting in an increased migration of carbon atoms to the boundaries, thus coarsening the carbides to sizes larger than the WAAM processed ones [62]. With larger carbides and more ferrite, wrought H13 has a lower hardness value than WAAM processed H13.

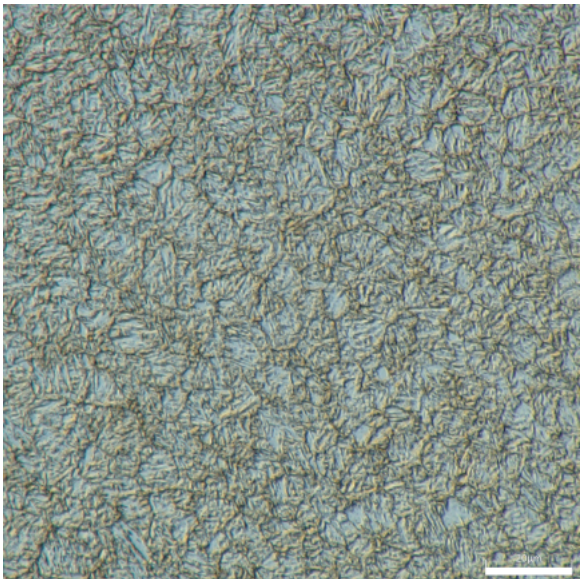

Figure 31: Microstructure of wrought H13 after tempering at 615 °C for 2 hours. The scale bars in this image is 20μm in length.

In summary, the tempering cycles both in the as-built state and after austenitizing were able to soften all four feedstocks down to the desirable range of 44 to 48 HRC. Both conditions experienced increased softening with increased tempering temperature due to internal stress relief and carbide coarsening. However, the as-built Dievar hardened when exposed to the first tempering cycle, so a secondary tempering cycle was used to achieve the desired hardness value. This is likely due to the growth of the carbides to the critical size causing an increase in strength due to secondary hardening. An additional temper or higher temperatures is necessary to overage the carbides so that they are incoherent with the matrix. The hardness values from the directly

tempered samples were on average higher than those of the conventionally heat-treated samples. The carbides before tempering were larger in the conventionally heat-treated samples, leading to an overall decrease in hardness. When compared to both WAAM processed H13, wrought tempered samples were softer due to larger carbide sizes and more ferrite regions.

Chapter 4: Conclusions

In this work two types of H13 feedstock, Dievar, and QRO 90 were printed using WAAM without the presence of cracks. Gas porosity and lack-of-fusion defects remained an issue, but can be remedied with proper preparation of the feedstock material and process optimization. All of the WAAM processed tool steels underwent a conventional heat treatment cycle and were able to achieve the desirable hardness range of 44 to 48 HRC. WAAM processed tool steels were also subjected to a single temper from the as-built state and achieved the same desired hardness range. In addition to these main conclusions, this work was able to demonstrate the following conclusions:

- Cored H13 wire feedstock performed similarly to the solid H13 wire feedstock. Slight differences in the austenitizing and tempering behavior are a result of the copper content in the H13 solid feedstock.
- Copper in H13 feedstock stabilized the austenite which resulted in more retained austenite contents than the graphite coated H13 cored feedstock.
- While the annealing procedure softened all four feedstocks, the columnar grain structure remained. It is necessary to increase the temperature and/or soak times to drive the recrystallization of equiaxed grains.
- Annealed WAAM processed tool steels can be hardened back to its as-built hardness.
- Increased austenitizing temperature resulted in an increase in hardness for both H13 feedstocks likely due to the strengthening of the martensite from carbide dissolution.
- Increased austenitizing temperature had no effect on the hardness for Dievar and QRO 90 feedstocks since the highly thermal stable carbides did not dissolve. A consistent carbon content remained in the austenite and thus the martensite was not strengthened.

- Most single tempers on the austenitized and as-built conditions were successful in achieving the desired hardness range of 44 to 48 HRC. The as-built Dievar was the only sample that did not soften to this range. A second tempering cycle was successful in softening the as-built Dievar to the desired hardness range.
- Increased tempering temperature resulted in a decrease in hardness for most of the tool steel feedstocks due to the depletion of carbon in the martensite, carbide coarsening, and relief of internal stresses from the martensitic transformation. The as-built Dievar experienced strengthening likely due to the carbides coarsening to the critical precipitate size.
- Wrought H13 consisted of fine, equiaxed grains while the WAAM processed H13 had large, columnar grains. The fine grains contributed to the higher hardness value after austenitizing when compared to the WAAM processed samples at the same condition. The fine grains increased the driving force of carbon diffusion to the carbides causing them to coarsen at a faster rate than the WAAM processed samples.

Chapter 5: Future Work

While hardness measurements correlate with the strength of the material, tensile properties are necessary to truly understand the mechanical properties of the material. Another property that is critical in casting applications is toughness. In high pressure die casting, dies need to have high toughness to prevent the formation of cracks from thermal fatigue at the tool surface [34]. To measure toughness, Charpy impact samples should be made and tested. Furthermore, due to the columnar grains anisotropy in mechanical properties is expected. Tensile and Charpy impact samples along the build direction and perpendicular to the build direction need to be created to evaluate the anisotropy. These tests must be carried out to truly understand the differences between the conventional heat treatment and the directly tempered heat treatment, the difference between cored and solid H13 feedstock, and the effect of copper on the mechanical properties. These mechanical properties should be compared to wrought values to determine if WAAM processed tool steels are superior to wrought tool steels.

The feedstock material and substrate material should be properly cleaned to eliminate the moisture and grease that create gas porosity. Process optimization must be done to eliminate the large lack-of-fusion defects because of their detrimental effect on mechanical performance. By varying the voltage and travel speed, the inputted powers that produce defect free microstructures would be revealed. Varying the wire feed rate is another parameter to look at as it determines how much is deposited per time interval. X-ray CT on each sample should be considered as it would be a more reliable tool in porosity detection than cross-sectioning.

Once a defect free microstructure is achieved, the microstructure of each tool steel should be evaluated with advanced characterization techniques. The identity and size of the carbides at each condition should be evaluated with SEM and EDS. For fine carbides TEM might be a more

trustworthy technique for identification and measurements. By understanding the distribution and size of the carbides, the differences in tempering response for the conventionally heat treated and directly tempered samples can be more definitively understood.

To have a complete understanding of the effect of copper on the microstructure and mechanical properties, feedstocks of the same material should have wires with and without a copper coating. For example, an additional H13 cored wire with a similar copper coating should be evaluated to provide a direct comparison. Additionally, wrought Dievar and QRO 90 samples should be evaluated and heat treated to compare with the WAAM processed feedstocks. Using XRD to quantitatively measure the retained austenite contents in all conditions would provide a better understanding of the effect of copper on the amount of retained austenite after heat treatments as well as how effective the single temper was in reducing the retained austenite content.

References

[1] D. L. Bourell and T. Wohlers, "Introduction to Additive Manufacturing," in *ASM Handbook. Volume 24: Additive Manufacturing Processes*, vol. 24, D. L. Bourell, W. Frazier, H. Kuhn, and M. Seifi, Eds. Materials Park, Ohio: ASM International, 2020.

[2] V. Bhavar, P. Kattire, V. Patil, S. Khot, K. Gujar, and R. Singh, "A review on powder bed fusion technology of metal additive manufacturing," Sep. 2014.

[3] S. C. Altıparmak and B. Xiao, "A market assessment of additive manufacturing potential for the aerospace industry," *J. Manuf. Process.*, vol. 68, pp. 728–738, Aug. 2021, doi: 10.1016/j.jmapro.2021.05.072.

[4] I. Astm, "ASTM52900-15 standard terminology for additive manufacturing—general principles—terminology," *ASTM Int. West Conshohocken PA*, vol. 3, no. 4, p. 5, 2015.

[5] S. Yin and R. Lupoi, "Introduction to Cold Spray Additive Manufacturing," in *Cold Spray Additive Manufacturing: From Fundamentals to Applications*, S. Yin and R. Lupoi, Eds. Cham: Springer International Publishing, 2021, pp. 1–7. doi: 10.1007/978-3-030-73367-4_1.

[6] I. Gibson, D. Rosen, and B. Stucker, "Directed Energy Deposition Processes," in *Additive Manufacturing Technologies: 3D Printing, Rapid Prototyping, and Direct Digital Manufacturing*, I. Gibson, D. Rosen, and B. Stucker, Eds. New York, NY: Springer, 2015, pp. 245–268. doi: 10.1007/978-1-4939-2113-3_10.

[7] T. A. Rodrigues, V. Duarte, R. M. Miranda, T. G. Santos, and J. P. Oliveira, "Current Status and Perspectives on Wire and Arc Additive Manufacturing (WAAM)," *Materials*, vol. 12, no. 7, p. 1121, Apr. 2019, doi: 10.3390/ma12071121.

[8] S. W. Williams, F. Martina, A. C. Addison, J. Ding, G. Pardal, and P. Colegrove, "Wire + Arc Additive Manufacturing," *Mater. Sci. Technol.*, vol. 32, no. 7, pp. 641–647, May 2016, doi: 10.1179/1743284715Y.0000000073.

[9] Y. Zou, "Cold Spray Additive Manufacturing: Microstructure Evolution and Bonding Features," *Acc. Mater. Res.*, vol. 2, no. 11, pp. 1071–1081, Nov. 2021, doi: 10.1021/accountsmr.1c00138.

[10] T. DebRoy *et al.*, "Additive manufacturing of metallic components – Process, structure and properties," *Prog. Mater. Sci.*, vol. 92, pp. 112–224, Mar. 2018, doi: 10.1016/j.pmatsci.2017.10.001.

[11] A. G. Colomo, D. Wood, F. Martina, and S. W. Williams, "A comparison framework to support the selection of the best additive manufacturing process for specific aerospace applications," *Int. J. Rapid Manuf.*, vol. 9, no. 2/3, p. 194, 2020, doi: 10.1504/IJRAPIDM.2020.107736.

[12] "Cold Spray: A guide to best practice.pdf." Arbegast Materials Processing and Joining Lab: South Dakota School of Mines and Technology, 2012.

[13] "SPEE3D Brochure." SPEE3D, 2022.

[14] S. Bagherifard and M. Guagliano, "Fatigue performance of cold spray deposits: Coating, repair and additive manufacturing cases," *Int. J. Fatigue*, vol. 139, p. 105744, Oct. 2020, doi: 10.1016/j.ijfatigue.2020.105744.

[15] "MX3D Bridge," *MX3D*. https://mx3d.com/industries/infrastructure/mx3d-bridge/ (accessed Sep. 13, 2022).

[16] "Tool Steels," Dec. 1998, doi: 10.31399/asm.hb.mhde2.a0003114.

[17] G. A. Roberts, G. Krauss, and R. Kennedy, "Chapter 2: Classification and Selection of Tool Steels," in *Tool Steels*, 5th ed., ASM International, 1998, pp. 7–28.

[18] F. Bonollo, N. Gramegna, and G. Timelli, “High-Pressure Die-Casting: Contradictions and Challenges,” *JOM*, vol. 67, no. 5, pp. 901–908, May 2015, doi: 10.1007/s11837-015-1333-8.
[19] V. Nunes, F. J. G. Silva, M. F. Andrade, R. Alexandre, and A. P. M. Baptista, “Increasing the lifespan of high-pressure die cast molds subjected to severe wear,” *Surf. Coat. Technol.*, vol. 332, pp. 319–331, Dec. 2017, doi: 10.1016/j.surfcoat.2017.05.098.
[20] A. Armillotta, R. Baraggi, and S. Fasoli, “SLM tooling for die casting with conformal cooling channels,” *Int. J. Adv. Manuf. Technol.*, vol. 71, no. 1, pp. 573–583, Mar. 2014, doi: 10.1007/s00170-013-5523-7.
[21] S. Feng, A. M. Kamat, and Y. Pei, “Design and fabrication of conformal cooling channels in molds: Review and progress updates,” *Int. J. Heat Mass Transf.*, vol. 171, p. 121082, Jun. 2021, doi: 10.1016/j.ijheatmasstransfer.2021.121082.
[22] J. Wang, S. Liu, Y. Fang, and Z. He, “A short review on selective laser melting of H13 steel,” *Int. J. Adv. Manuf. Technol.*, vol. 108, no. 7, pp. 2453–2466, Jun. 2020, doi: 10.1007/s00170-020-05584-4.
[23] “Thermal-fatigue behaviour of hot-work tool steels: Metals Technology: Vol 8, No 1.” https://www.tandfonline.com/doi/abs/10.1179/030716981803275947 (accessed Sep. 14, 2022).
[24] T. Wang, Y. Zhang, Z. Wu, and C. Shi, “Microstructure and properties of die steel fabricated by WAAM using H13 wire,” *Vacuum*, vol. 149, pp. 185–189, Mar. 2018, doi: 10.1016/j.vacuum.2017.12.034.
[25] Y. Ali, P. Henckell, J. Hildebrand, J. Reimann, J. P. Bergmann, and S. Barnikol-Oettler, “Wire arc additive manufacturing of hot work tool steel with CMT process,” *J. Mater. Process. Technol.*, vol. 269, pp. 109–116, Jul. 2019, doi: 10.1016/j.jmatprotec.2019.01.034.
[26] J. Ge *et al.*, “Wire-arc additive manufacturing H13 part: 3D pore distribution, microstructural evolution, and mechanical performances,” *J. Alloys Compd.*, vol. 783, pp. 145–155, Apr. 2019, doi: 10.1016/j.jallcom.2018.12.274.
[27] W. Hackenhaar, J. A. E. Mazzaferro, C. C. P. Mazzaferro, N. Grossi, and G. Campatelli, “Effects of different WAAM current deposition modes on the mechanical properties of AISI H13 tool steel,” *Weld. World*, Jul. 2022, doi: 10.1007/s40194-022-01342-0.
[28] A. N. M. Tanvir *et al.*, “Phase stability and mechanical properties of wire + arc additively manufactured H13 tool steel at elevated temperatures,” *J. Mater. Sci. Technol.*, vol. 67, pp. 80–94, Mar. 2021, doi: 10.1016/j.jmst.2020.04.085.
[29] J. G. Speer and R. J. Gaster, “Austenitizing in Steels,” Aug. 2013, doi: 10.31399/asm.hb.v04a.a0005786.
[30] J. L. Dossett and H. E. Boyer, “2. Fundamentals of Heat Treating Steel,” in *Practical Heat Treating*, 2nd ed., ASM International, 2016, pp. 9–25.
[31] R. N. Penha, L. C. F. Canale, J. Vatavuk, and S. Lampman, “Tempering of Steels,” Aug. 2013, doi: 10.31399/asm.hb.v04a.a0005815.
[32] D. Rosen and S. Kim, “Design and Manufacturing Implications of Additive Manufacturing,” in *ASM Handbook. Volume 24: Additive Manufacturing Processes*, vol. 24, D. L. Bourell, W. Frazier, H. Kuhn, and M. Seifi, Eds. Materials Park, Ohio: ASM International, 2020.
[33] “Technical Data Sheet for Dievar Electrode.” Uddeholm, 2017.
[34] R. A. Mesquita, R. Schneider, and C. S. Gonçalves, “Heat Treating of Hot-Work Tool Steels,” in *Heat Treating of Irons and Steels*, J. L. Dossett and G. E. Totten, Eds. ASM International, 2014, pp. 336–346. doi: 10.31399/asm.hb.v04d.a0005974.

[35] “Technical Data Sheet for QRO 90.” Uddeholm, 2011.
[36] “Technical Data Sheet for Eureka 31 Flux Cored Wire Electrode.” Eureka Welding Alloys, 2013.
[37] “Technical Data Sheet for Eureka 31 Electrode.” Eureka Welding Alloys, 2013.
[38] “NX-2.20 Surface Tension Transfer (STT).” Lincoln Electric.
[39] A01 Committee, “Specification for Tool Steels Alloy,” ASTM International. doi: 10.1520/A0681-08R22.
[40] S. Kou, *Welding metallurgy*, 2nd ed. Hoboken, N.J: Wiley-Interscience, 2003.
[41] J.-Y. Kang *et al.*, “Effect of copper addition on the characteristics of high-carbon and high-chromium steels,” *Mater. Sci. Eng. A*, vol. 614, pp. 36–44, Sep. 2014, doi: 10.1016/j.msea.2014.07.004.
[42] P. Edwards, A. O’Conner, and M. Ramulu, “Electron beam additive manufacturing of titanium components: Properties and performance,” *J. Manuf. Sci. Eng.*, vol. 135, no. 6, 2013, doi: 10.1115/1.4025773.
[43] B. Wu *et al.*, “A review of the wire arc additive manufacturing of metals: properties, defects and quality improvement,” *J. Manuf. Process.*, vol. 35, pp. 127–139, Oct. 2018, doi: 10.1016/j.jmapro.2018.08.001.
[44] J. L. Huang, N. Warnken, J.-C. Gebelin, M. Strangwood, and R. C. Reed, “On the mechanism of porosity formation during welding of titanium alloys,” *Acta Mater.*, vol. 60, no. 6, pp. 3215–3225, Apr. 2012, doi: 10.1016/j.actamat.2012.02.035.
[45] S. Li *et al.*, “Microstructures and mechanical properties of Al–Zn–Mg aluminium alloy samples produced by wire+arc additive manufacturing,” *J. Mater. Res. Technol.*, vol. 9, no. 6, pp. 13770–13780, Nov. 2020, doi: 10.1016/j.jmrt.2020.09.114.
[46] W. j. Sames, F. Medina, W. h. Peter, S. s. Babu, and R. r. Dehoff, “Effect of Process Control and Powder Quality on Inconel 718 Produced Using Electron Beam Melting,” in *8th International Symposium on Superalloy 718 and Derivatives*, John Wiley & Sons, Ltd, 2014, pp. 409–423. doi: 10.1002/9781119016854.ch32.
[47] F. Wang, S. Williams, P. Colegrove, and A. A. Antonysamy, “Microstructure and Mechanical Properties of Wire and Arc Additive Manufactured Ti-6Al-4V,” *Metall. Mater. Trans. A*, vol. 44, no. 2, pp. 968–977, Feb. 2013, doi: 10.1007/s11661-012-1444-6.
[48] C. E. Seow, H. E. Coules, G. Wu, R. H. U. Khan, X. Xu, and S. Williams, “Wire + Arc Additively Manufactured Inconel 718: Effect of post-deposition heat treatments on microstructure and tensile properties,” *Mater. Des.*, vol. 183, p. 108157, Dec. 2019, doi: 10.1016/j.matdes.2019.108157.
[49] L. Wang, J. Xue, and Q. Wang, “Correlation between arc mode, microstructure, and mechanical properties during wire arc additive manufacturing of 316L stainless steel,” *Mater. Sci. Eng. A*, vol. 751, pp. 183–190, Mar. 2019, doi: 10.1016/j.msea.2019.02.078.
[50] B. Baufeld, E. Brandl, and O. van der Biest, “Wire based additive layer manufacturing: Comparison of microstructure and mechanical properties of Ti–6Al–4V components fabricated by laser-beam deposition and shaped metal deposition,” *J. Mater. Process. Technol.*, vol. 211, no. 6, pp. 1146–1158, Jun. 2011, doi: 10.1016/j.jmatprotec.2011.01.018.
[51] H. L. Wei, J. Mazumder, and T. DebRoy, “Evolution of solidification texture during additive manufacturing,” *Sci. Rep.*, vol. 5, no. 1, p. 16446, Nov. 2015, doi: 10.1038/srep16446.

[52] S. Morito, H. Tanaka, R. Konishi, T. Furuhara, and T. Maki, "The morphology and crystallography of lath martensite in Fe-C alloys," *Acta Mater.*, vol. 51, no. 6, pp. 1789–1799, Apr. 2003, doi: 10.1016/S1359-6454(02)00577-3.
[53] George Vander Voort, "Revealing the Microstructure of Tool Steels," *Vacaero*, Mar. 15, 2012. https://vacaero.com/information-resources/metallography-with-george-vander-voort/1174-revealing-the-microstructure-of-tool-steels.html (accessed Oct. 25, 2022).
[54] Y. Huang, G. Cheng, S. Li, and W. Dai, "Precipitation Behavior of Large Primary Carbides in Cast H13 Steel," *Steel Res. Int.*, vol. 90, no. 7, p. 1900035, 2019, doi: 10.1002/srin.201900035.
[55] J. Ge, J. Lin, Y. Chen, Y. Lei, and H. Fu, "Characterization of wire arc additive manufacturing 2Cr13 part: Process stability, microstructural evolution, and tensile properties," *J. Alloys Compd.*, vol. 748, pp. 911–921, Jun. 2018, doi: 10.1016/j.jallcom.2018.03.222.
[56] C. Chen *et al.*, "Effect of Heat Treatment on Microstructure and Mechanical Properties of Laser Additively Manufactured AISI H13 Tool Steel," *J. Mater. Eng. Perform.*, vol. 26, no. 11, pp. 5577–5589, Nov. 2017, doi: 10.1007/s11665-017-2992-0.
[57] G. A. Roberts, G. Krauss, and R. Kennedy, "Chapter 4: Tool Steel Alloy Design," in *Tool Steels*, 5th ed., ASM International, 1998, pp. 45–65.
[58] G. A. Roberts, R. Kennedy, and G. Krauss, *Tool Steels, 5th Edition*. ASM International, 1998.
[59] G. Asala, J. Andersson, and O. A. Ojo, "Improved dynamic impact behaviour of wire-arc additive manufactured ATI 718Plus®," *Mater. Sci. Eng. A*, vol. 738, pp. 111–124, Dec. 2018, doi: 10.1016/j.msea.2018.09.079.
[60] H. L. Cai, P. J. Du, H. L. Yi, and D. Wu, "Effects of Austenitizing Temperature on Microstructure and Properties of Hot-Formed Steel," *Adv. Mater. Res.*, vol. 1063, pp. 88–92, 2015, doi: 10.4028/www.scientific.net/AMR.1063.88.
[61] G. A. Roberts, G. Krauss, and R. Kennedy, "Chapter 13: Hot-Work Tool Steels," in *Tool Steels*, 5th ed., ASM International, 1998, pp. 219–243.
[62] W. D. Callister and D. G. Rethwisch, *Materials Science and Engineering: an Introduction*, 9th edition. Hoboken, NJ: Wiley, 2014.
[63] A. Rajasekhar, G. Madhusudhan Reddy, T. Mohandas, and V. S. R. Murti, "Influence of austenitizing temperature on microstructure and mechanical properties of AISI 431 martensitic stainless steel electron beam welds," *Mater. Des.*, vol. 30, no. 5, pp. 1612–1624, May 2009, doi: 10.1016/j.matdes.2008.07.042.
[64] "Effects of carbon and nitrogen on austenite stability and tensile deformation behavior of 15Cr-15Mn-4Ni based austenitic stainless steels," *Mater. Sci. Eng. A*, vol. 742, pp. 608–616, Jan. 2019, doi: 10.1016/j.msea.2018.11.048.
[65] K. Nakashima, K. Imakawa, Y. Futamura, T. Tsuchiyama, and S. Takaki, "Effect of copper addition on grain growth behavior of austenite in low carbon steels," *Mater. Sci. Forum*, vol. 467–470, no. II, pp. 905–910, 2004, doi: 10.4028/www.scientific.net/msf.467-470.905.
[66] G. A. Roberts, G. Krauss, and R. Kennedy, "Chapter 5: Principles of Tool Steel Heat Treatment," in *Tool Steels*, 5th ed., ASM International, 1998, pp. 67–86.
[67] E. Pippel, J. Woltersdorf, G. Pöckl, and G. Lichtenegger, "Microstructure and Nanochemistry of Carbide Precipitates in High-Speed Steel S 6-5-2-5," *Mater. Charact.*, vol. 43, no. 1, pp. 41–55, Jul. 1999, doi: 10.1016/S1044-5803(99)00003-0.

[68] J. E. Bridge, G. N. Maniar, and T. V. Philip, “Carbides in M-50 high speed steel,” *Metall. Mater. Trans. B*, vol. 2, no. 8, pp. 2209–2214, Aug. 1971, doi: 10.1007/BF02917552.
[69] D. A. Porter, K. E. Easterling, and K. E. Easterling, *Phase Transformations in Metals and Alloys (Revised Reprint)*, 3rd ed. Boca Raton: CRC Press, 2009. doi: 10.1201/9781439883570.
[70] G. Hoyle, *High Speed Steels*. Butterworths, 1988. Accessed: Oct. 27, 2022. [Online]. Available: https://scholar.google.com/scholar?hl=en&as_sdt=0%2C5&q=+Hoyle%2C+G.+High+Speed+Steels%2C+1988+Butterworths+&btnG=
[71] C. Højerslev, “Tool steels,” Risø National Laboratory, Roskilde, Report 87-550-2833–0, 2001.
[72] H.-J. Yi, J.-W. Kim, Y.-L. Kim, and S. Shin, “Effects of Cooling Rate on the Microstructure and Tensile Properties of Wire-Arc Additive Manufactured Ti–6Al–4V Alloy,” *Met. Mater. Int.*, vol. 26, no. 8, pp. 1235–1246, Aug. 2020, doi: 10.1007/s12540-019-00563-1.
[73] M. Katancik, S. Mirzababaei, M. Ghayoor, and S. Pasebani, “Selective laser melting and tempering of H13 tool steel for rapid tooling applications,” *J. Alloys Compd.*, vol. 849, p. 156319, Dec. 2020, doi: 10.1016/j.jallcom.2020.156319.
[74] L. D. Barlow and M. Du Toit, “Effect of Austenitizing Heat Treatment on the Microstructure and Hardness of Martensitic Stainless Steel AISI 420,” *J. Mater. Eng. Perform.*, vol. 21, no. 7, pp. 1327–1336, Jul. 2012, doi: 10.1007/s11665-011-0043-9.
[75] Y. Xie, X. Cheng, J. Wei, and R. Luo, “Characterization of Carbide Precipitation during Tempering for Quenched Dievar Steel,” *Materials*, vol. 15, no. 18, Art. no. 18, Jan. 2022, doi: 10.3390/ma15186448.
[76] M. Grujicic, “Coherent precipitation of M2C carbides in AF1410 steel,” *Mater. Sci. Eng. A*, vol. 117, pp. 215–220, Sep. 1989, doi: 10.1016/0921-5093(89)90103-2.
[77] Z. Liu, C. Liu, L. Miao, X. Guo, J. Ding, and H. Zhang, “The Evolution of Complex Carbide Precipitates in a Low Alloy Cr–Mo–V Steel after Long-Term Aging Treatment,” *Materials*, vol. 12, no. 10, Art. no. 10, Jan. 2019, doi: 10.3390/ma12101724.
[78] Y. Shi, X. Wu, J. Li, and N. Min, “Tempering stability of Fe–Cr–Mo–W–V hot forging die steels,” *Int. J. Miner. Metall. Mater.*, vol. 24, no. 10, pp. 1145–1157, Oct. 2017, doi: 10.1007/s12613-017-1505-3.
[79] G. E. Dieter, *Mechanical Metallurgy*, 3rd ed. New York: McGraw-Hill, 1986.

Appendix A: Austenitizing Curves

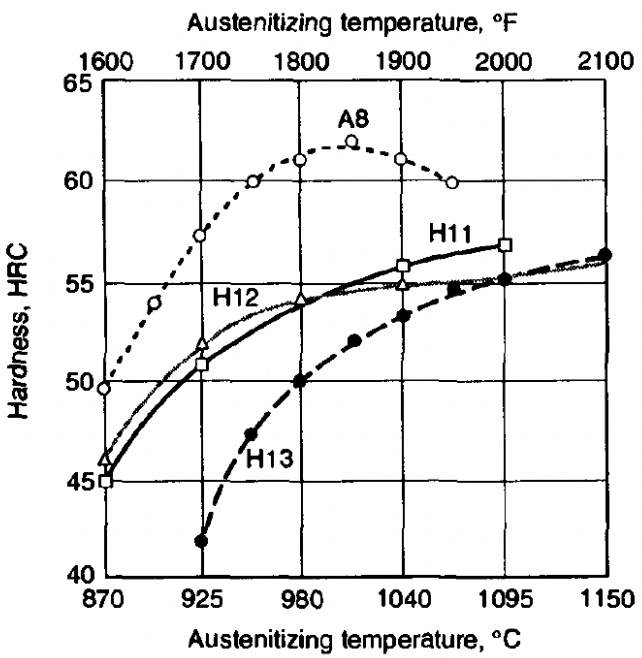

Figure 32: Effect of austenitizing temperature on hardness of hot-work chromium tool steels [61].

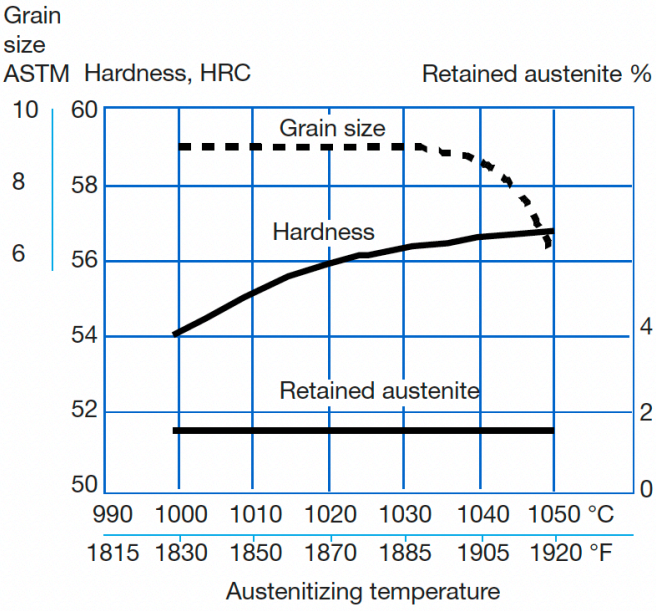

Figure 33: Hardness, grain size, and retained austenite as functions of austenitizing temperature for Uddeholm Dievar [33].

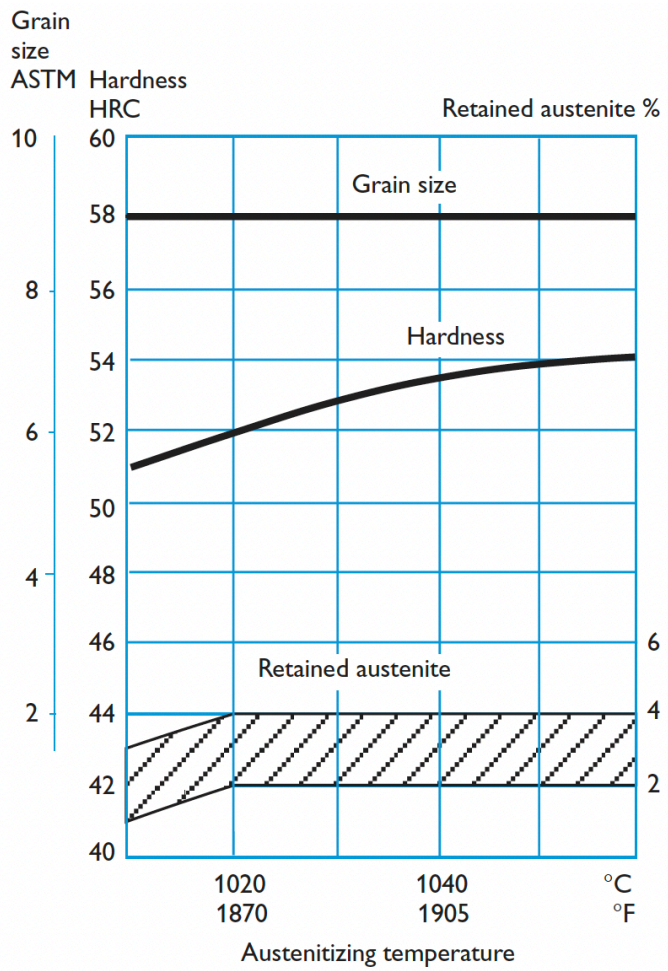

Figure 34: Hardness, grain size, and retained austenite as functions of austenitizing temperature for Uddeholm QRO 90 [35].

Appendix B: Tempering Curves

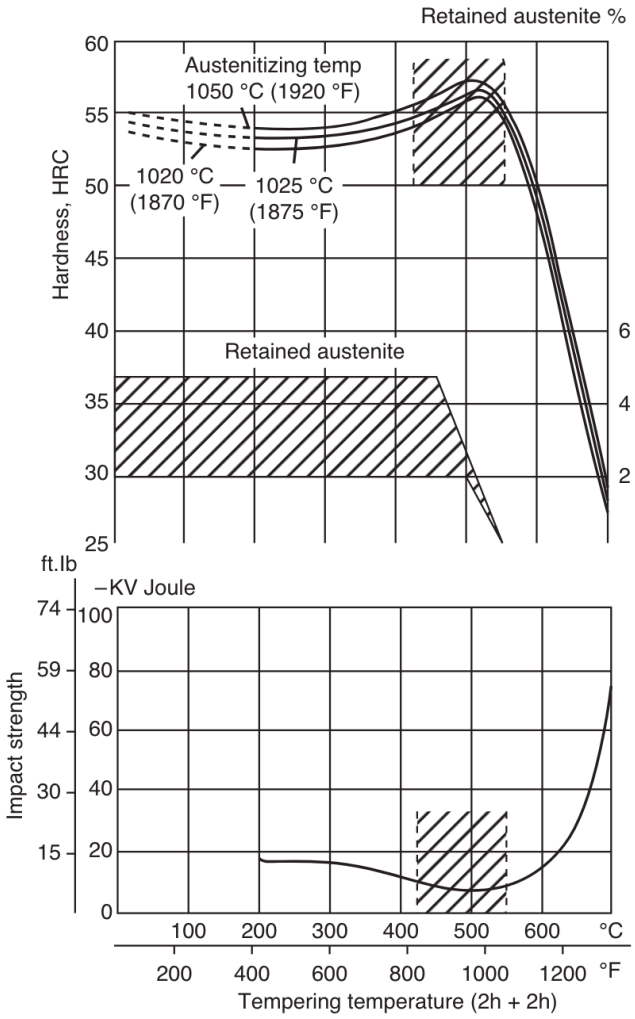

Figure 35: Tempering curves for H13 tool steel [34].

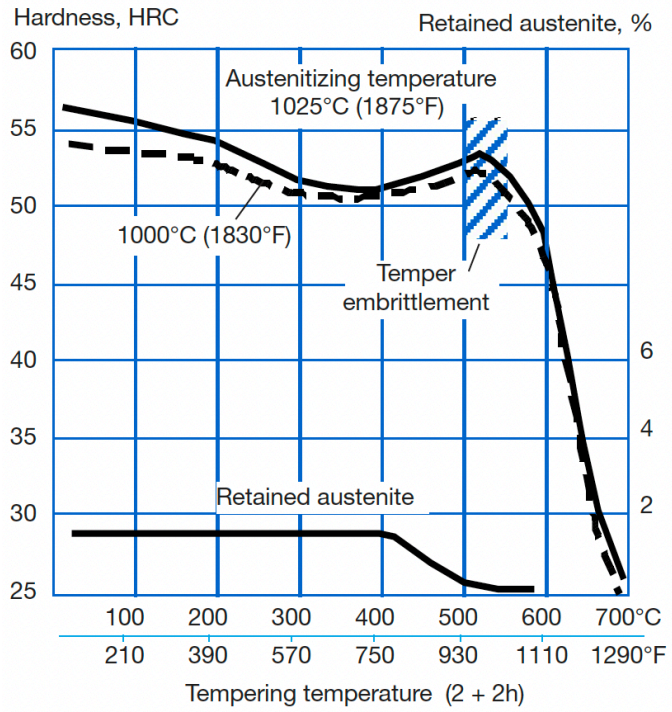

Figure 36: Tempering curves for Uddeholm Dievar [33].

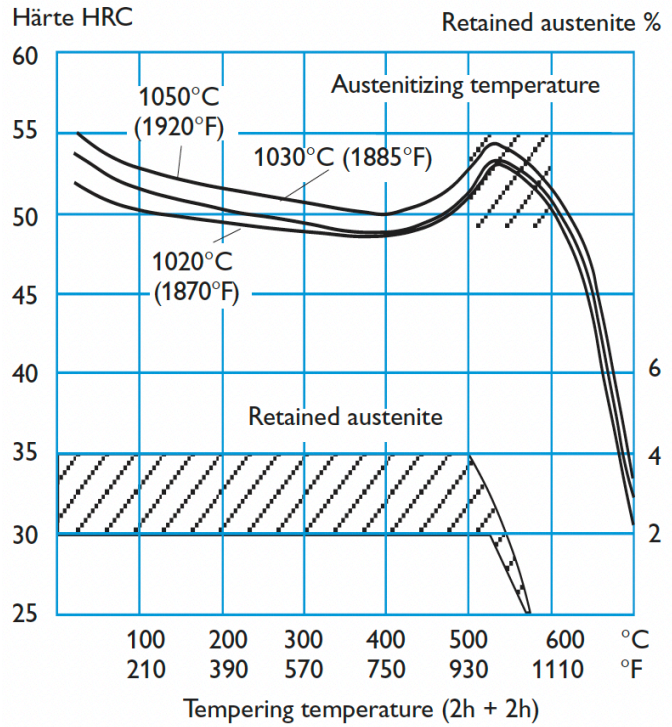

Figure 37: Tempering curves for Uddeholm QRO 90 Supreme [35].

Appendix C: Bright field images of the as-built condition

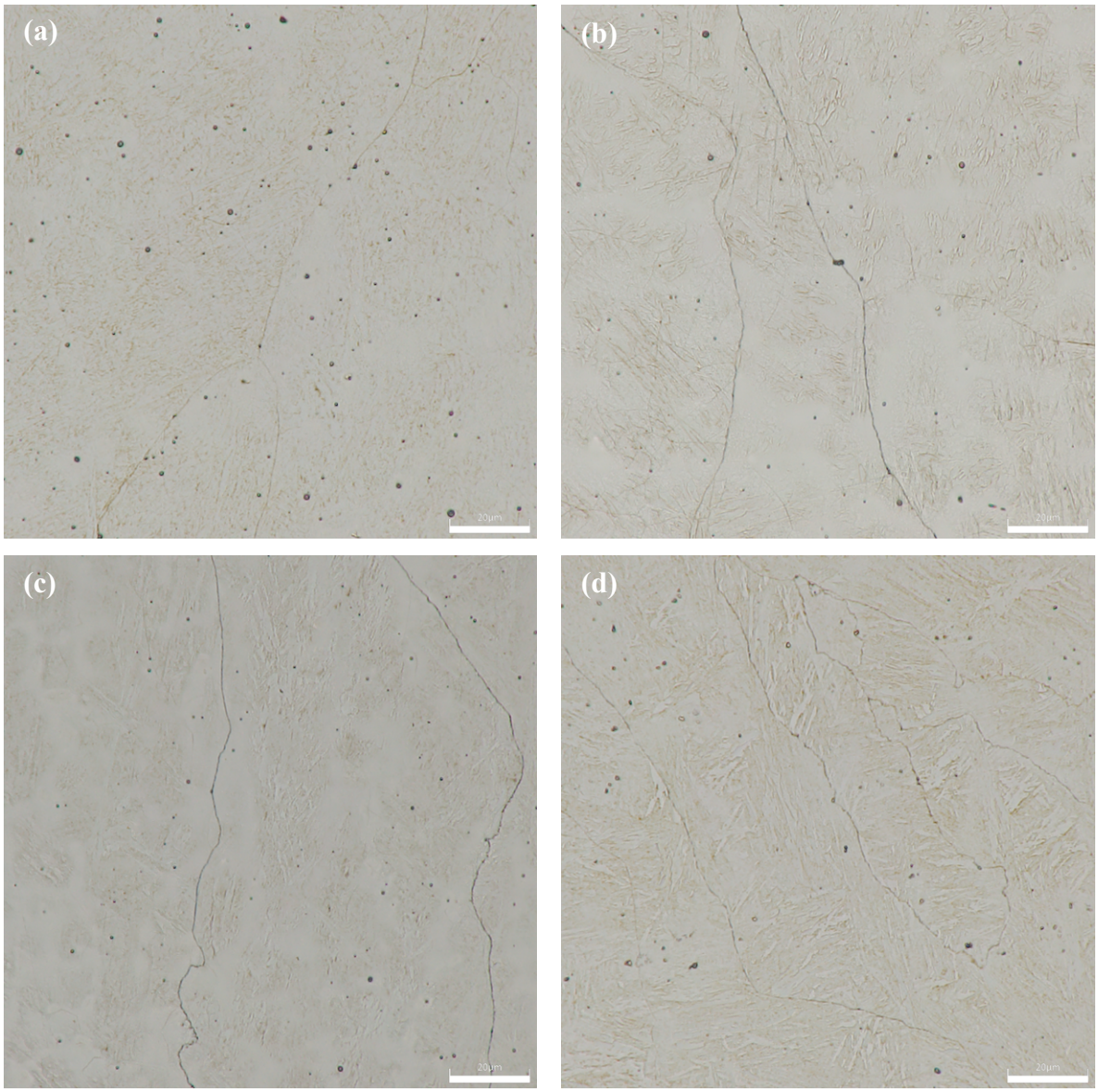

Figure 38: Etched microstructures of (a) H13 cored, (b) H13 solid, (c) Dievar, and (d) QRO 90 at 2000X using bright field imaging to show the smooth white network regions. The scale bars on each image are 20μm in length.